iScience

Article

A particle-scale study showing microwave energy can effectively decarbonize process heat in fluidization industry

Graphical abstract

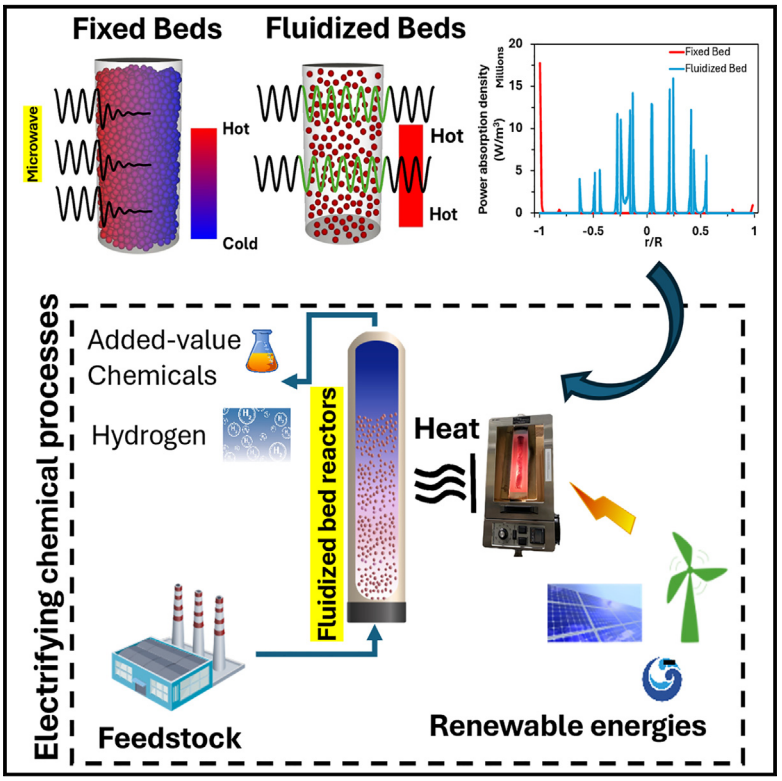

Highlights

- Research offers new perspectives on uniform microwave heating for industrial use
- Fluidized particles overcome limited penetration depth, with no field attenuation
- Over 90% uniformity in microwave heating of fluidized beds with Geldart A and B
- Particle collisions generate localized hotspots, enhancing microwave absorption

Authors

Mehdi Salakhi, Murray J. Thomson

Correspondence

murray.thomson@utoronto.ca

In brief

Heat transfer; Electromagnetics; Engineering

Salakhi & Thomson, 2025, iScience *28*, 111732
February 21, 2025
https://doi.org/10.1016/j.isci.2024.111732

CellPress

iScience

CellPress
OPEN ACCESS

Article

A particle-scale study showing microwave energy can effectively decarbonize process heat in fluidization industry

Mehdi Salakhi[1] and Murray J. Thomson[1,2,*]
[1]Department of Mechanical & Industrial Engineering, University of Toronto, Toronto, ON M5S 3G8, Canada
[2]Lead contact
*Correspondence: murray.thomson@utoronto.ca
https://doi.org/10.1016/j.isci.2024.111732

SUMMARY

Microwave heating converts electromagnetic energy directly into thermal energy within the heated material, thereby overcoming the limitations of traditional indirect heat transfer methods. However, microwaves are well-known to have limited penetration depth, which remains a significant challenge that inhibits the use of microwaves in processes requiring uniform heating. Here, we show that fluidized beds of particles with sufficient electrical conductivity break the limitations imposed by microwave penetration depth, enabling uniform heating in large-scale reactors. Results suggest that the alternating magnetic field penetrates the entire studied reactor to induce eddy currents everywhere, causing each particle to be heated. The power absorption density for Geldart A and B particles across the bed is uniform, with no evidence of exponential attenuation, introducing unexpected penetration depth under the magnetic field component. Utilizing microwave energy, sourced by clean electricity, to heat fluidized beds offers a transformative solution to decarbonize industry, significantly reducing greenhouse gas emissions.

INTRODUCTION

The industrial sector accounts for approximately 25% of the direct CO_2 emissions from global energy-related processes.[1] To keep global temperature rise below 1.5°C, it is necessary to reduce these emissions by 80% by 2050.[2] Currently, the industrial sector is the largest energy consumer, using 149 million terajoules, with only about 20% of this energy sourced from electricity. Recent estimates indicate that up to 50% of the fuel consumption for the energy industry needs could potentially be replaced by electrification using only current technologies.[3] Therefore, transitioning industrial units from fossil fuel energy to clean electricity can drastically accelerate decarbonization efforts.[4]

Among the industrial units, fluidized beds, commonly heated through fossil fuel combustion, have been widely utilized in a diverse set of applications such as chemical processing, energy production, material synthesis, mineral processing, pharmaceutical, and food industries.[5] Fluidized beds offer key advantages, including superior heat and mass transfer, uniform mixing, and continuous operation.[6,7] Provided by renewable sources of electricity, electrically heated fluidized beds (EHFBs) are emerging as a viable solution to achieve the electrification of the industry units. This shift can significantly reduce CO_2 emissions and improve overall energy efficiency.[8]

In this regard, microwave heating plays an integral role in developing EHFBs. Microwave heating provides unique advantages over conventional methods by directly converting electromagnetic (EM) energy into thermal energy within the material being heated. Moreover, the rapid and targeted heating of microwaves can significantly enhance traditional processes, resulting in a marked increase in both productivity and energy efficiency, as evidenced by recent experimental studies.[9–14] However, it is well established that as microwave penetrates a material, its intensity exponentially decays, limiting the use of microwave energy primarily to small-scale applications.[15]

Integrating the primary advantages of fluidized beds and microwave heating presents an exciting opportunity for the development of reactors in chemical processes and energy production units.[8] Recently, several experimental studies have come to light by exploiting microwave heating of fluidized bed reactors.[16–22] Despite this, the literature still lacks a sufficient understanding of microwave-fluidization interaction mechanisms owing to challenges in temperature, electric current, and EM field measurements in a microwave experimental apparatus.[23–25] This knowledge gap hinders the broader application of microwave energy in industrial settings.[15,26] To date, it is unclear how microwaves interact with a dense set of fluidized particles.

Detailed modeling investigations are needed to bridge the gap and expand the utilization of microwave technology for more commercial and scientific purposes. In this regard, the interaction of EM waves with metal powders or packed beds can be found in the literature.[27,28] However, particle-scale modeling of the interaction between microwaves and fluidized beds is scarce due to the complexities inherent in such inhomogeneous media and demanding computational resources.

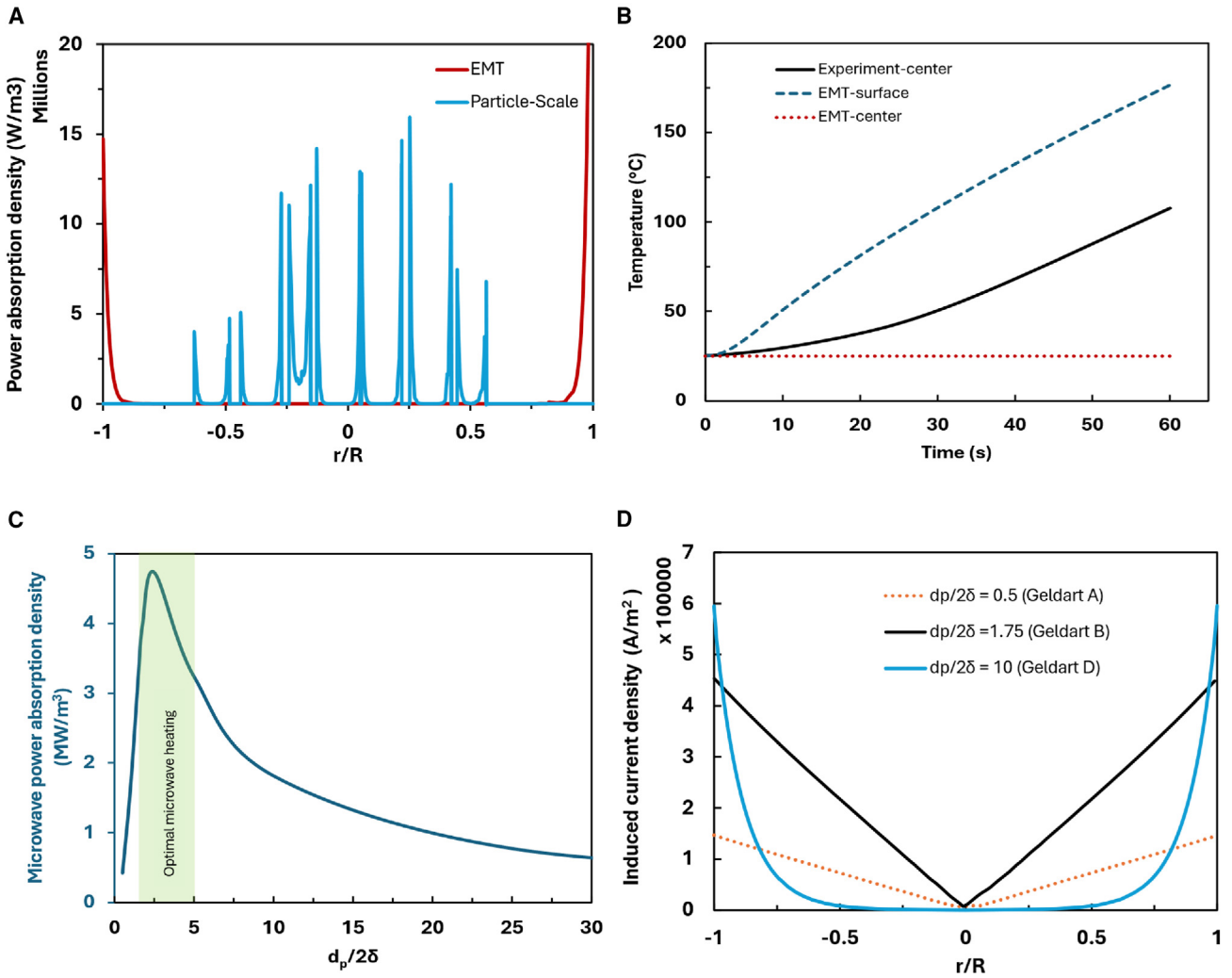

Figure 1. Key insights from particle-scale analysis of microwave absorption in fluidized particles

(A) Distribution of power absorption density across the 1-inch diameter of the bed using EMT approach and particle-scale study for Geldart D particles.

(B) Comparison of local temperature at the center and surface of the bed between experimental measurements from Dadsetan et al.[16] and modeling using the EMT approach.

(C) Power absorption density as a function of particle size and skin depth, suggesting $d_p/2\delta$ between 1.5 and 5 for an optimal microwave heating. According to this, maximum microwave heating occurs at $d_p/2\delta = 2.5$.

(D) Magnitude of the resultant induced current density within the particle for three various particle sizes corresponding to Geldart A, B, and D. The data in (D) are plotted along a line spanning the diameter of the particle.

Our previous work[16] successfully combined microwave heating with a fluidized bed of carbon particles to produce CO_2-free hydrogen from methane pyrolysis. In this process, fluidized carbon particles absorb microwave energy and create a hot medium for methane to decompose into hydrogen and solid carbon. The resulting solid carbon covers the surface of the existing carbon particles. However, the role of fluidization, microwave interaction, and the evolution of microwave penetration depth are not yet fully understood.

Here, we aim to study the underlying heating and coupling mechanisms between microwave and fluidization of our covered carbon particles. Our study presents a pioneering numerical analysis of microwave heating in fluidized beds with 10,000 micron-sized particles—a scale and configuration not previously explored in the literature. For this purpose, a detailed particle-scale model, capable of solving Maxwell's equations across scales from the macroscopic cavity level down to micron-sized particles, is developed to establish a comprehensive understanding of the process. The developed model is then used to advance the science behind microwave energy absorption in fluidized beds containing particles of Geldart A (100 μm), B (350 μm), and D (2 mm), investigating different particle sizes commonly utilized in fluidized beds. Afterward, we explore the effect of fluidized versus packed beds on microwave penetration depth, which delivers new observations regarding the role of fluidization. Furthermore, the interaction of electric and magnetic fields with

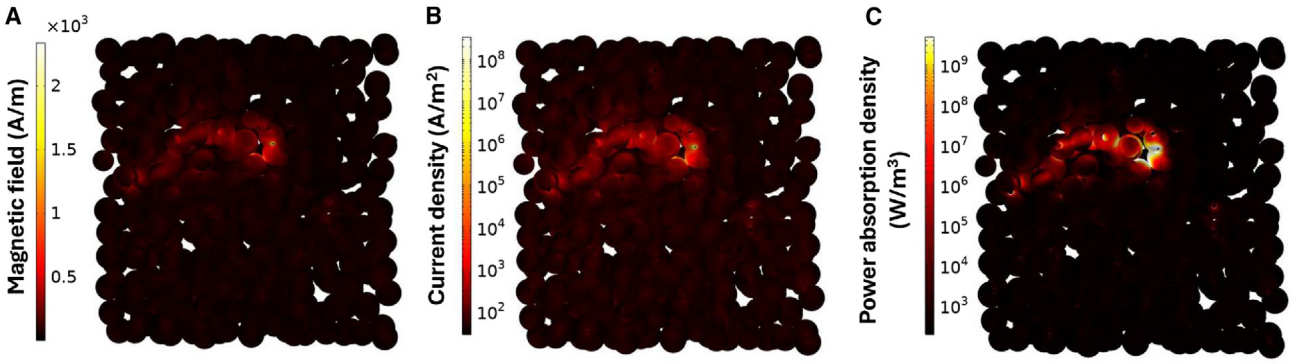

Figure 2. Effect of particle collisions and contacts during fluidization on the microwave interaction with Geldart D particles

(A) Magnetic field.

(B) Induced current density.

(C) Power absorption density.

The plots are the snapshots of the middle layer of the bed.

the emulsion phase and bubbles during fluidization of each particle group is examined. We introduce unexpected penetration depth in fluidized beds heated under the magnetic field component, providing promising microwave energy insights for chemical and energy processes requiring uniform heating.

RESULTS AND DISCUSSION

Key insights from particle-scale analysis of microwave absorption in a set of fluidized particles

In studying the EM behavior of heterogeneous materials, effective medium theory (EMT) and particle-scale models are two prevalent methodologies used. EMT simplifies the complex microstructure of a composite material by approximating it as a homogeneous medium with averaged properties, while particle-scale models can capture detailed interactions and local variations, providing accurate predictions of EM behavior in complex materials.[29,30]

Figure 1A compares the radial distribution of power absorption density across the 1-inch diameter bed obtained from the EMT approach, Bruggeman's model in Equation 13, and the particle-scale model. For the particle-scale model, the bed is filled with particles classified as Geldart D. According to Figure 1A, the EMT approach predicts a very low penetration depth where only the outer layer of the bed can be heated effectively by microwaves. In contrast, the particle-scale study reveals a greater penetration of microwaves as each pair of peaks belongs to a single particle, leading to microwave heating absorption of each particle within the 1-inch bed.

Furthermore, solving the heat transfer Equation 12 for the EMT approach suggests only surface heating of the bed where the surface temperature of the bed reaches around 170°C, while the center remains cold during the 60 s of microwave heating, as can be seen in Figure 1B. The results of the EMT approach contradict the experimental temperature rise seen in Figure 1B, where the thermocouple was placed in the center of the bed 3 cm above the bottom of the reactor. Therefore, the current EMT model fails to capture the physics behind the microwave heating of fluidized beds. The particle-scale study, on the other hand, unveils that the entire carbon bed is heated by microwave heating, confirming the thermal behavior observed experimentally. We conclude that the developed particle-scale model is a powerful tool to capture intricate details involved in the microwave heating of fluidized particles.

It is essential to first establish a single-particle heating study. The single-particle heating study can potentially shed insights into the microwave heating of fluidized beds. It can unveil the effect of particle size on heating and demonstrate the interactions of the particles with the magnetic and electric components of the EM field. To this end, a single carbon particle is placed in the microwave cavity. Thus, the particle can be irradiated by microwaves from all directions. Figures 1C and 1D depict the heating performance of a single carbon particle irradiated by microwaves under different sizes.

From a microwave power absorption standpoint, Figure 1C indicates that, if the particle size is much smaller than the skin depth, the microwave power partially transmits through the particle and does not dissipate. If the particle size is much larger than the skin depth, the particle mostly reflects the incident microwave and does not fully absorb it. On the other hand, if the particle size is comparable to the skin depth, $d_p/2\delta$ between 1.5 and 5, the microwave heating absorption is optimum and efficient as highlighted in green in Figure 1A. The power absorption density curve shown in Figure 1C suggests that the peak microwave heating occurs when $d_p/2\delta = 2.5$, which is consistent with the findings for conductive metal powders reported by Ignatenko et al.[31] Therefore, our semiconductive carbon particles behave like conductive materials at the particle level. The single-particle study reveals that the average size of the covered carbon particles ($d_p/2\delta = 1.75$) used in our microwave heating process[32] falls within the optimal microwave absorption region, confirming the efficient absorption of the microwave observed experimentally by Dadsetan et al.[16]

When a particle is exposed to microwaves, an electric current is induced within it. Figure 1D shows the distribution of resultant

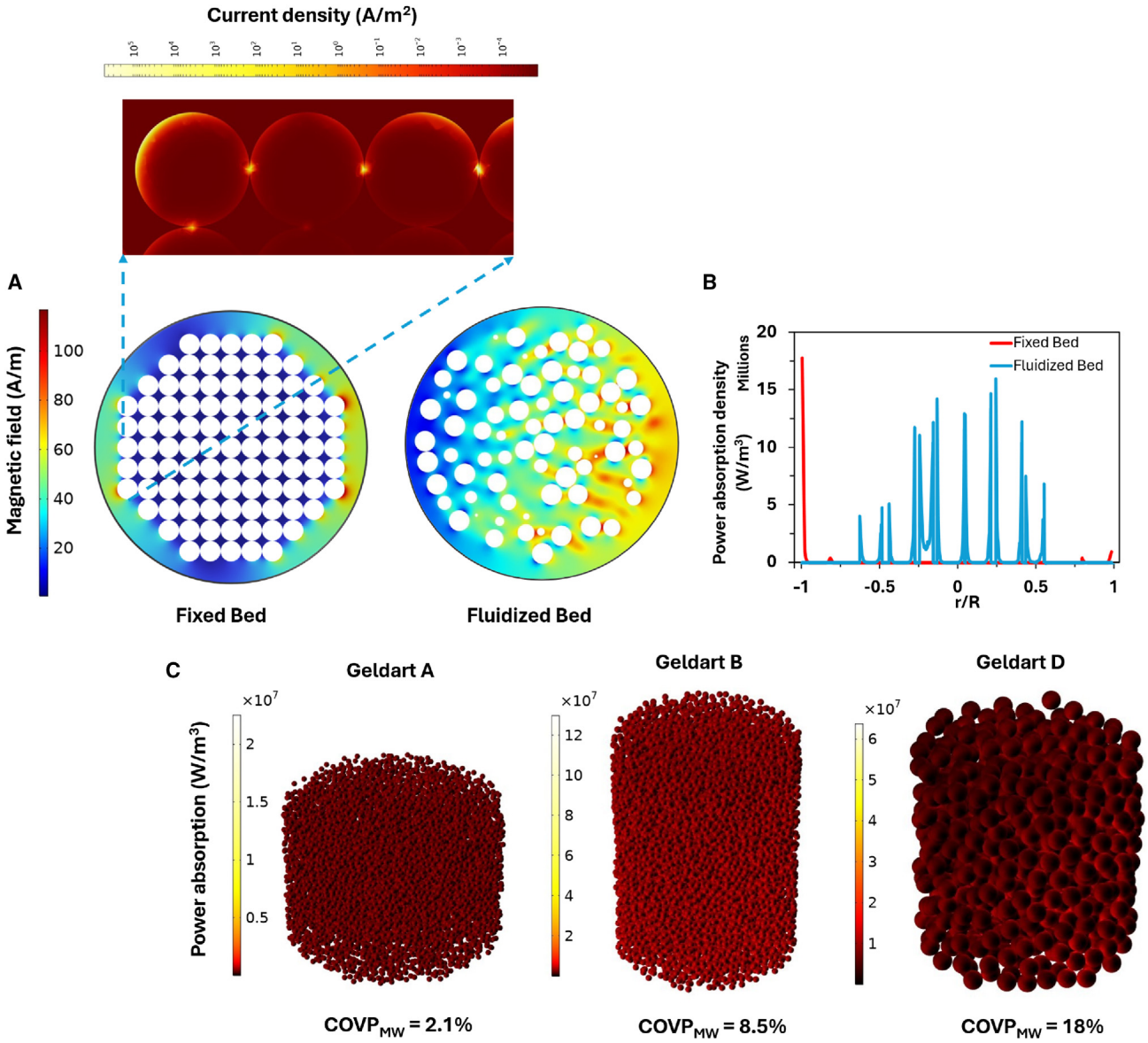

Figure 3. The effect of fluidization on the distribution of the EM field and penetration depth

(A) Comparison of the magnetic field penetration between a fixed bed and a fluidized bed. The magnetic field plots represent the top view of the middle layer of the bed.

(B) Distribution of power absorption density between a fixed bed and a fluidized bed using Geldart D particles.

(C) Power absorption density of each particle in a fluidized state, considering particle groups Geldart A, B, and D.

Data variability is represented as the coefficient of variation, $COVP_{MW}$, calculated as SD/mean × 100 based on numerical simulation results.

induced current density within our carbon particle. For Geldart A and B particles, where the particle size is comparable to the skin depth, the induced current is linearly spread over the entire volume of the particle rather than being concentrated near the surface (Geldart D in Figure 1D). The trend seen in Figure 1D suggests that this spreading results in a lower current density. For instance, the current density at the surface of Geldart D is 6×10^5 A/m^2, dropping to 4.5×10^5 and 1.5×10^5 A/m^2 for Geldart B and A, respectively. The induced current density distribution determines the interparticle mutual interaction when dealing with a bed of particles. These interactions can influence the heating pattern and efficiency, as the EM fields from one particle can affect the induced currents in nearby particles. The rigorous analysis discussed and provided in Tables S3 and S4 reveals that the induced current, as depicted in Figure 1D, is suppressed when the particle size is comparable to or smaller than the skin depth (Geldart A and B in this case). More importantly, solid volume fraction exhibits a negligible effect on the microwave absorption of individual Geldart A and B carbon particles, as shown in Figure S2 and Table S4. This finding suggests that, at the

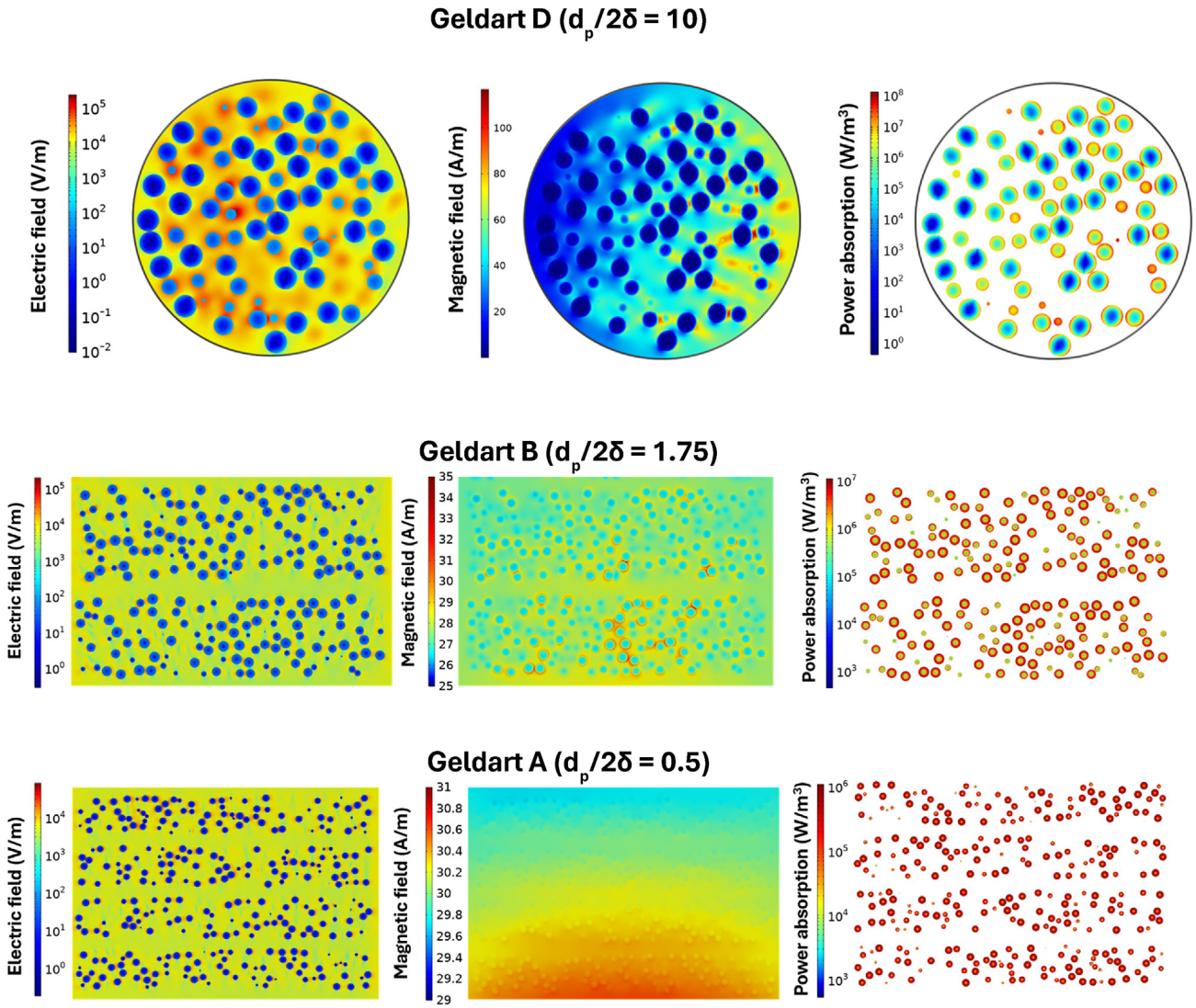

Figure 4. Power absorption density and interaction of the EM field with the fluidized bed of particle groups Geldart A, B, and D

To have a better visualization for the fluidization of Geldart D particles, the plots present the top view of the middle layer, while the side view of the middle layer is displayed for Geldart A and B particles.

studied reactor scale placed within a 2.45 GHz microwave cavity, a fluidized bed of Geldart A and B particles may behave as a collection of independent absorbing particles when exposed to microwaves. However, it is critical to explore how microwave penetration depth affects the power absorption of individual particles.

Particle collisions with the help of magnetic field enhance microwave absorption

As shown in Figure S3, the locations of the formed hot and cold spots align with the magnetic field pattern, suggesting that the magnetic field component of microwaves is responsible for heating our covered carbon particles. The heating rates, displayed in Figure S5, further support this conclusion. The average heating rate is 6.2°C/s when the fluidized bed of Geldart B particles is placed in the maximum magnetic field (H field) of the microwave, compared to 0.8°C/s when placed in the maximum electric field (E field). These data indicate that the bed of our carbon particles effectively couples with the magnetic field rather than the electric field, regardless of particle size. This behavior contrasts with typical microwave heating processes, where heating primarily occurs due to the electric field.[8] Given this, we particularly study the interaction of the magnetic field with the fluidized particles.

In any fluidization process, frequent collision of particles leads to the formation of contact points.[33] Figure 2 explores the effect of contact points between the particles during fluidization on microwave interaction and absorption. To this end, a random collision is introduced by defining a distance equal to the particle size d_p, resulting in a minimum contact area.

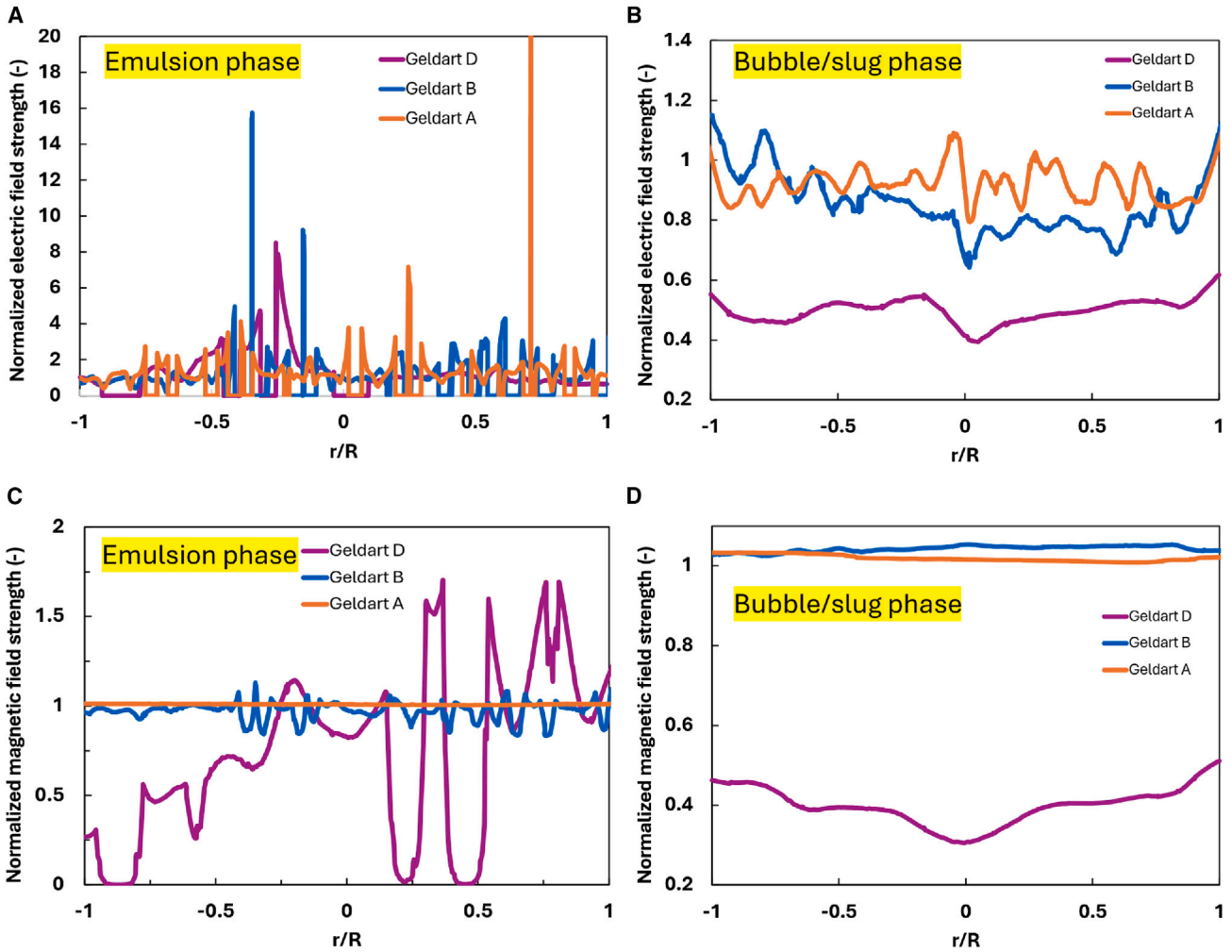

Figure 5. Interaction of electric and magnetic fields with the emulsion phase and bubbles/slugs during fluidization of Geldart A, B, and D particles

(A) Normalized electric field strength in the emulsion phase.
(B) Normalized electric field strength in the bubble phase.
(C) Normalized magnetic field strength in the emulsion phase.
(D) Normalized magnetic field strength in the bubble phase.
The EM fields are normalized by the results of the corresponding empty cavity. All the graphs are plotted along a line spanning the bed's diameter.

Figure 2A illustrates that the magnetic field intensity is significantly higher at the contact points. The peak magnetic field occurs at the contact points of particles with a maximum of almost 2,600 A/m, which is about 18 times stronger than the maximum magnetic norm of 142 A/m observed for the fluidization without any contact points, as shown in Figure S6. As a result of this, Figure 2B reveals a highly non-uniform current distribution, with differences spanning several orders of magnitude and higher current densities of $>10^8$ A/m^2 at the contact points. These contact points between particles act as constriction resistance that concentrates the current flow, which faces a substantial resistance at the contacts due to the reduced contact area between particles.

This gives rise to an intense power absorption density exceeding 10^9 W/m^3, which is shown as glowing regions in Figure 2C, causing intense Joule heating and the formation of localized hotspots. Figure 2C also suggests that the network of particle contacts creates pathways for current flow, spreading the formed hotspot across the adjacent particles in contact as can be seen in Figures 2B and 2C. Several experimental studies have reported higher fuel conversion rates with microwave heating compared to conventional ones due to the formation of small hotspots/micro-plasmas inside catalytic beds.[9,34–36] Our study also confirms the formation of local hotspots in our process. Hence, it is plausible that the frequent presence of these small, localized hotspots, resulting from particle collisions, facilitates chemical reactions. This phenomenon likely contributes to the higher methane conversion rates observed and reported in our previous experiments.[16]

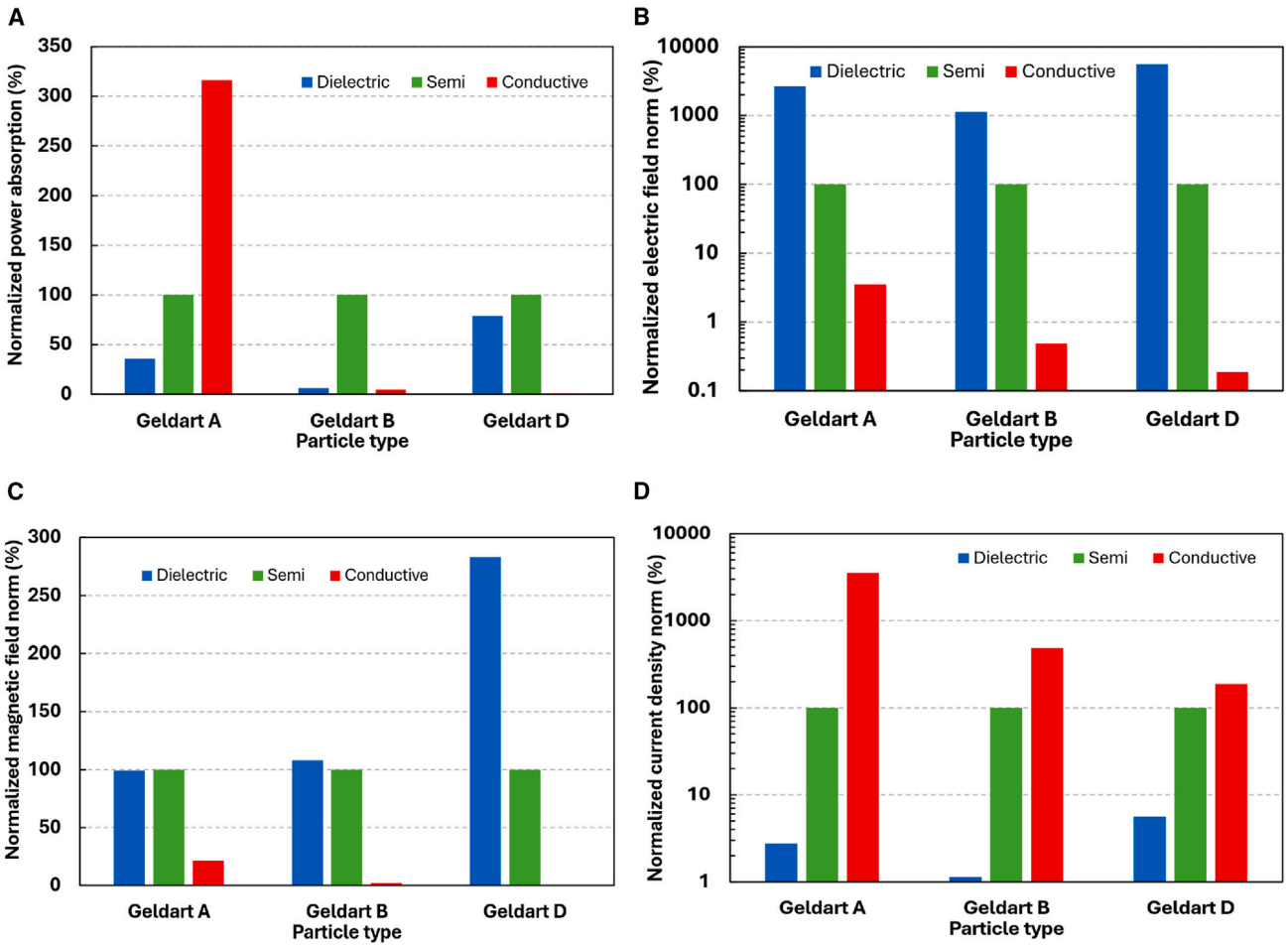

Figure 6. Effect of electrical conductivity on microwave heating absorption and EM field interaction with a fluidized bed of particle groups Geldart A, B, and D

(A) Normalized microwave heating absorption.

(B) Normalized electric field strength.

(C) Normalized magnetic field strength.

(D) Normalized current density.

All parameters are averaged over the bed of particles and normalized with respect to the semiconductive case.

Fluidization breaks the barrier of limited microwave penetration depth

In the context of microwave-heated fluidized beds, it is essential to comprehend the role of fluidization in the penetration and distribution of the field. To investigate this, the propagation of the magnetic field within a bed of Geldart D particles is compared in Figure 3A between a fixed bed, where all particles are touching each other, and a fluidized bed.

In the case of the fixed bed, the magnetic field attenuates rapidly to zero after the first layer of particles, suggesting that the fixed bed behaves like a solid block of a conductive material, reflecting the magnetic field as shown in Figure 3A. As previously discussed in Figure 2, when particles come into contact, they form conductive networks. The simulation, illustrated in Figure 3A, suggests that the current density is highly concentrated at the contact points of these networks. Consequently, this increased electrical conductivity significantly increases the resistance to microwave penetration, resulting in rapid attenuation. This modeling observation aligns well with the experimental findings on the microwave heating of metal powders of Fe_3O_4 documented by Amini et al.[37] The attenuation rate for fixed beds is also dependent on the ratio $d_p/2\delta$ of the particles. Particles with a lower $d_p/2\delta$ ratio will exhibit lower attenuation rates, allowing more layers of particles to be heated.

Unlike fixed beds, the dynamic nature of fluidized particles creates gaps that prevent the formation of conductive networks, boosting the propagation and penetration of the magnetic field, as shown in Figure 3A. The presence of these gaps in the fluidization reduces the overall electrical conductivity. This causes the bed to behave more like a dielectric material at the bulk level. Furthermore, Figure 3B demonstrates that fluidization significantly enhances microwave heating efficiency and uniformity compared to a fixed bed. The profile of power absorption density

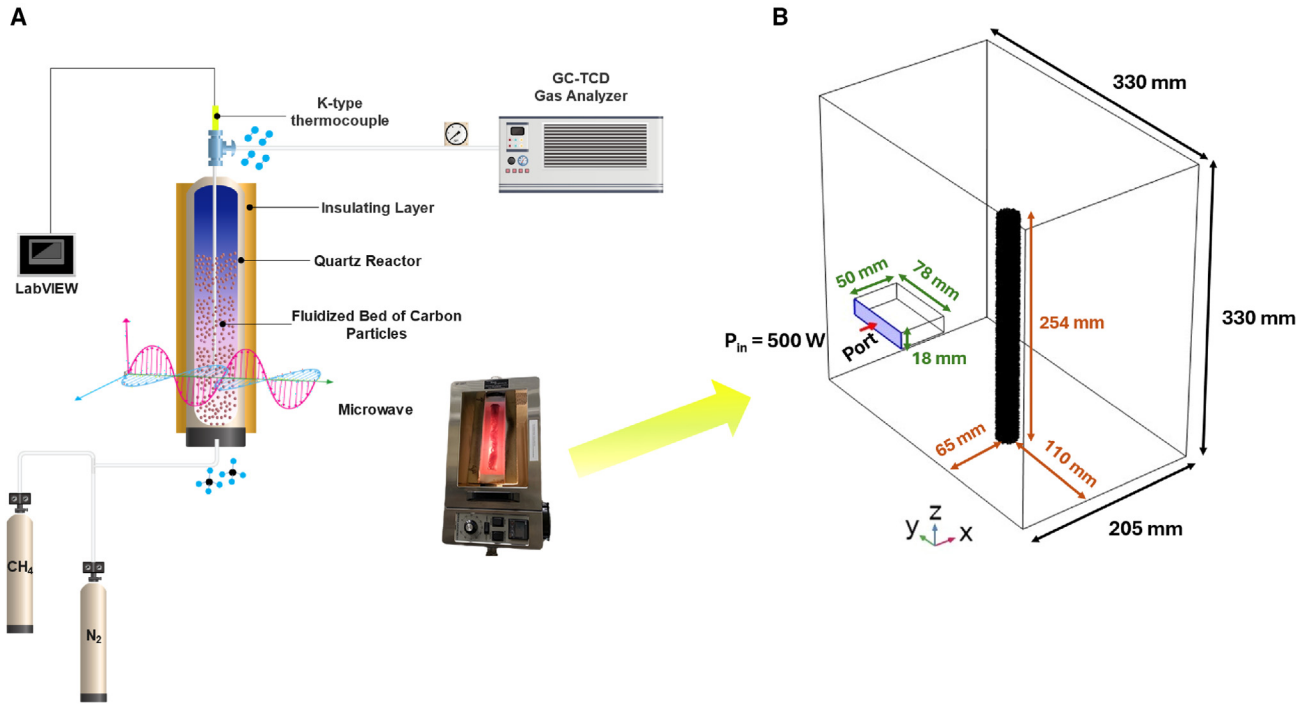

Figure 7. Microwave heating of our fluidized bed reactor of carbon particles

(A) Schematic of the bench-scale experiment.

(B) Simulated geometry of the cavity, waveguide, and the 1-inch fluidized bed reactor.

for the fixed bed in Figure 3B indicates that only the outer layer of the bed can be heated, which limits the penetration depth. However, in a fluidized state, the constant movement and dispersion of particles create pathways for microwaves to propagate without attenuation, overcoming the limitations of microwave penetration depth. This results in more uniform heating, with each particle contributing to the overall microwave heating of the bed, as illustrated by the peaks in blue in Figure 3B.

Figure 3C quantitatively and visually shows the uniformity of the heating pattern for Geldart A, B, and D particles in a fluidized state. It should be noted that, for this purpose, a shorter bed height is modeled for Geldart D particles ($<\lambda/4$) to minimize the effect of microwave hotspots on heating uniformity. A coefficient of variation (COV) of 18%, obtained from Equation 11, for Geldart D particles indicates that there is some degree of interparticle mutual interactions due to a high ratio $d_p/2\delta$ of 10.

The statistical analysis confirms the independent absorption of Geldart A and B particles by showing a low COV of 2.1% and 8.5%, respectively. Moreover, this finding supports the idea that the penetration depth in our microwave heating process of Geldart B particles extends beyond that in the studied 1-inch reactor in our experiments. Although the microwave heating of Geldart A particles is very uniform, their heating efficiency is low due to the small ratio of $d_p/2\delta$. In other words, microwave heating of Geldart A particles with a $d_p/2\delta$ of 0.5 is not within the optimal range of the power absorption density, as depicted in Figure 1A.

Figure 3C highlights that, in a fluidized bed of Geldart A and B particles, the bulk heating across the bed is uniform. This uniformity arises from the independent formation of eddy currents within each particle, ensuring consistent thermal distribution throughout the bed. Within the scale of our interest, there is no evidence of exponential attenuation in the power absorption density in the studied fluidized beds. This conclusion raises an interesting point for energy sectors that require uniform and efficient heating of fluids. With this, we envision significant academic and industrial opportunities to explore ways of implementing microwave energy in large-scale fluidized bed reactors.

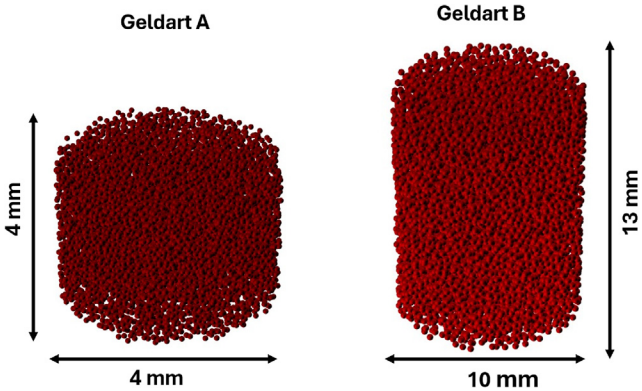

Figure 8. Round bed size used for the fluidization of Geldart A and B particles, containing almost 10,000 particles

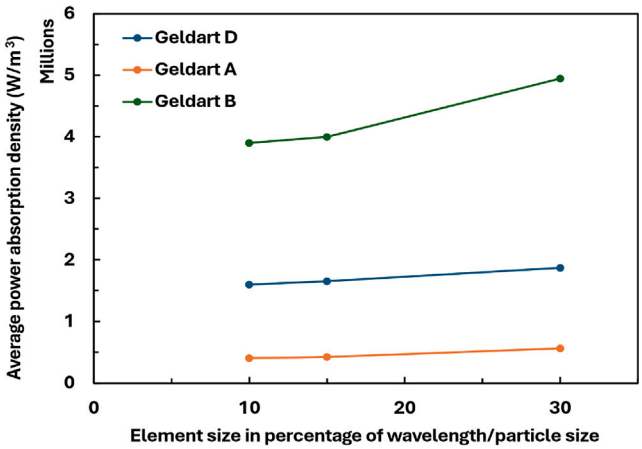

Figure 9. Grid sensitivity analysis for particle groups of Geldart A, B, and D as a function of microwave wavelength and particle size

Interaction of electric and magnetic fields with fluidized beds of Geldart A, B, and D

Figure 4 shows that, for all particle groups, particle regions belong to a low electric field intensity region, while the air surrounding the particles possesses several orders of magnitude higher electric field intensity region. This is because air has lower permittivity than our solid carbon particles. Moreover, several resonances of the electric field can be spotted exactly in the small gaps between closely spaced particles, with the electric field norm exceeding 10^5 V/m in these regions. The electric field plot of Geldart D particles in Figure 4 vividly shows that the individual resonance modes can interact and combine to form new resonance modes, spreading over the bed.

As can be seen in the magnetic field plots of Figure 4, significant and frequent magnetic resonance occurs only with Geldart D particles, where the magnetic field strength can surpass 100 A/m. In contrast, a few weak magnetic resonances are present between the small gaps of closely packed Geldart B particles, indicated by reddish regions in Figure 4, where the magnetic field norm reaches about 35 A/m. For Geldart A particles, on the other hand, magnetic resonance does not take place. The magnetic field distribution clearly illustrates that the fluidized bed of Geldart A particles is magnetically transparent, as the magnetic field inside the bed is almost indistinguishable from the external magnetic field. This suggests that microwave penetration for Geldart A particles, where the particle size is smaller than the skin depth, is remarkably higher than that for the other groups.

For Geldart A and B particles, the magnetic field infiltrates into the fluidized bed with almost no attenuation. Two reasons can be speculated for observing such a phenomenon. First, these particles possess a smaller or comparable ratio of $d_p/2\delta$, which mitigates the skin depth effect. Additionally, the non-magnetic nature of both particles and the air gaps between them further contributes to this minimal attenuation of the magnetic field.

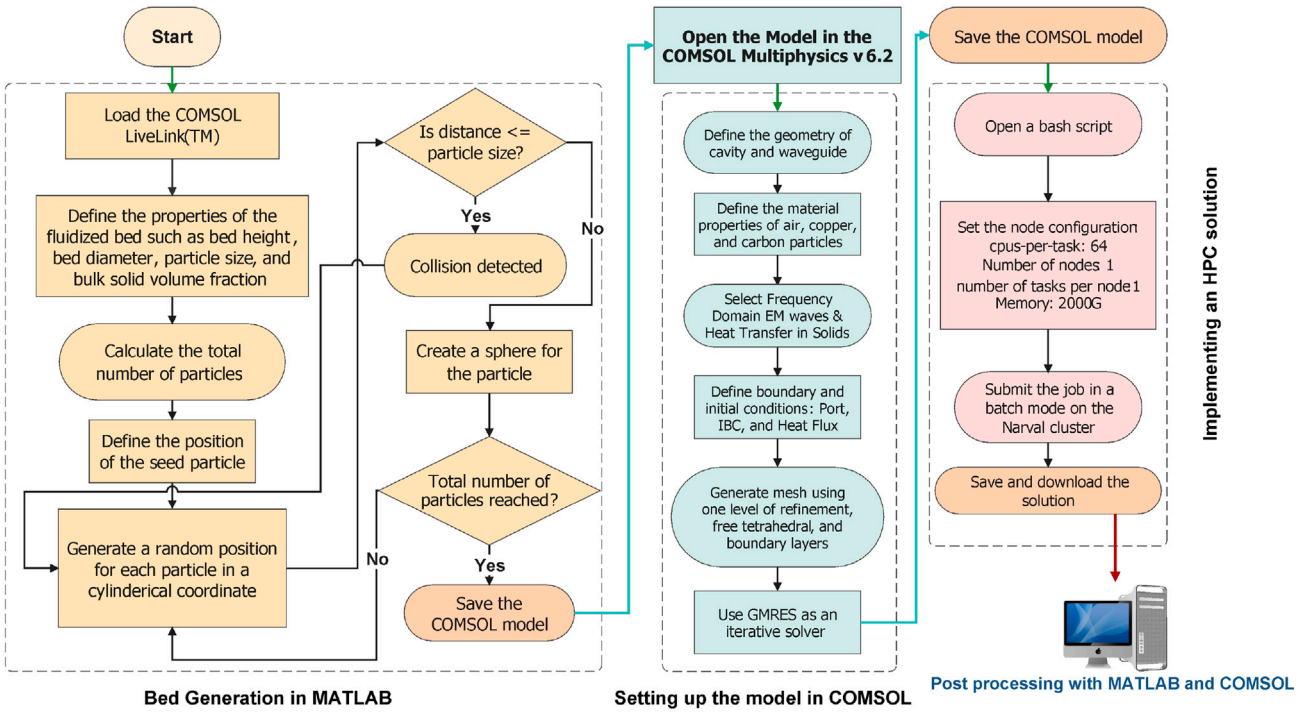

Figure 10. Flowchart of the implemented computational framework to conduct particle-scale simulations of microwave heating of fluidized beds

A High Performance computing (HPC) solution is implemented on the Narval cluster.[56]

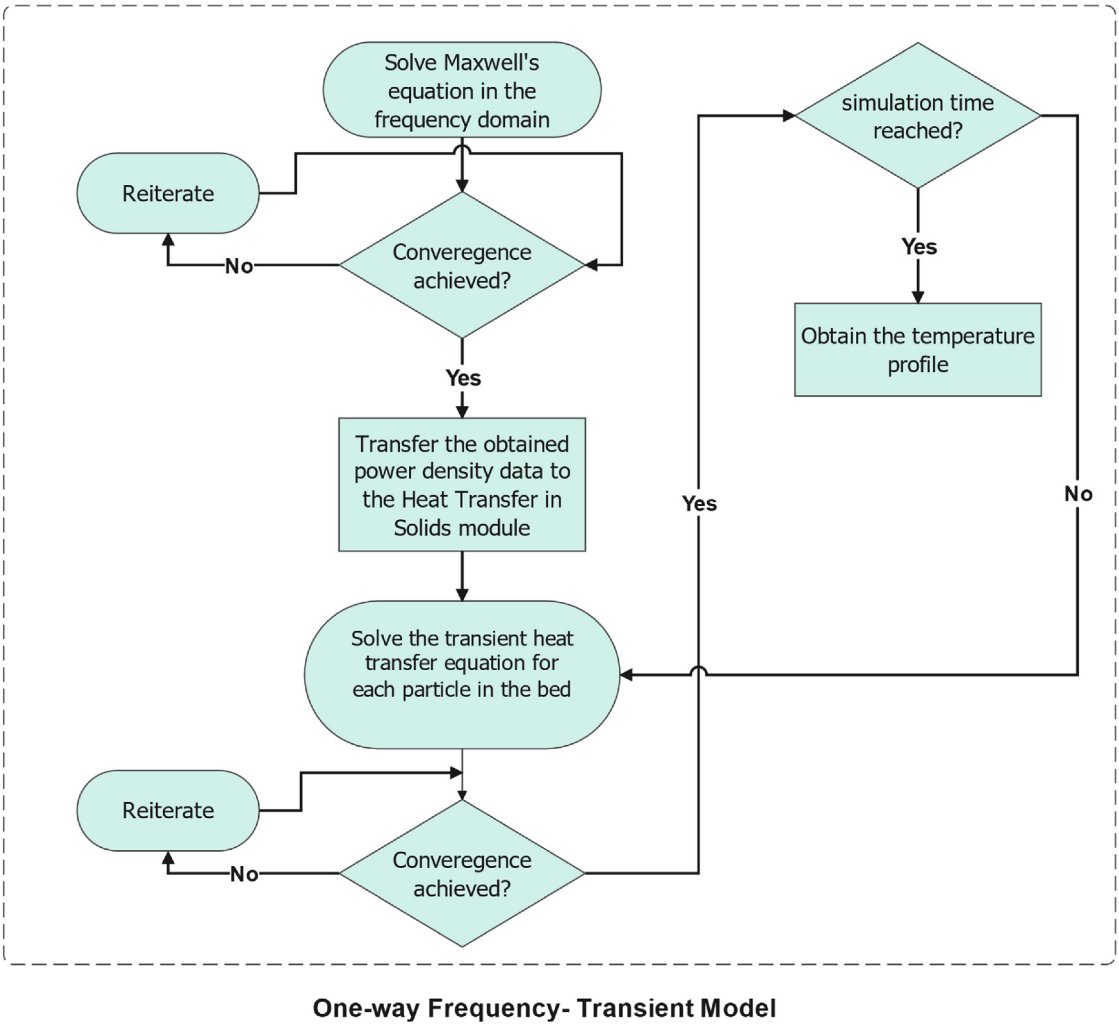

Figure 11. One-way frequency-transient model used in the present study to couple Maxwell's equation in frequency domain with the transient heat transfer equation

This observation also provides a fundamental explanation for the interaction of microwaves with powdered metals, as reported in the experimental work by Yoshikawa et al.[38] They found that non-magnetic metal powders experienced efficient microwave heating, in contrast to bulk metals, when exposed to the magnetic component of microwaves in a single-mode cavity.

Magnetic field strength for Geldart D particles decreases from right to left due to its sinusoidal oscillation nature. It is obvious that the trend of power absorption density is consistent with the sinusoidal evolution of the corresponding magnetic field. Therefore, particles on the right side absorb more power compared to those on the left. Moreover, the formation of a skin layer on each Geldart D particle is evident, where the power absorption density exponentially decays from above 10^8 W/m^3 at the surface to almost zero at the center of each Geldart D particle. The skin depth effect is less pronounced in Geldart A and B particles. Notably, the cross-section view of the power absorption density for Geldart A particles highlights the fact that each particle is uniformly heated throughout by microwave energy.

As reported by Dadsetan et al.,[16] our fluidization process operates at the bubbling regime. In bubbling fluidization, the bed consists of two primary phases: the bubble phase and the emulsion phase. The former contains mostly gas with very few particles, while the latter has a high concentration of solid particles. Under our condition, bubbles can grow to a size comparable to the bed diameter, potentially forming slugs.[39] Hence, bubbles and slugs can be used interchangeably in the present study. Given this, a region of bubbles/slugs with no particles is deliberately defined for each particle group by the bed diameter and a length of twice the corresponding particle size. Figure 5 quantitatively characterizes the interaction of EM waves with the bubble and the emulsion phases containing Geldart A, B, and D particles. The results are normalized by the strength of the EM fields obtained from the corresponding empty cavity depicted in Figure S4.

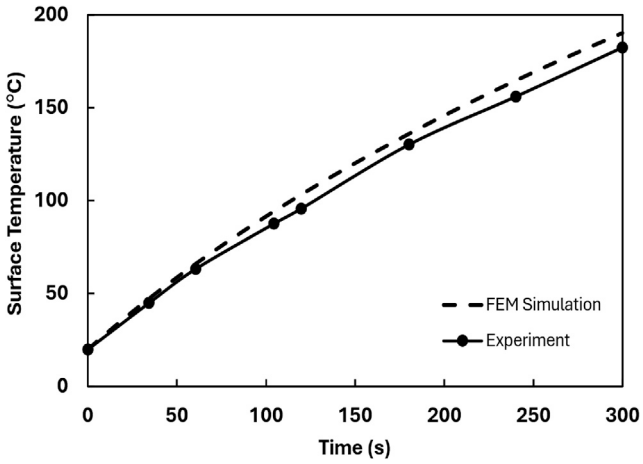

Figure 12. Comparison of our Finite Element Solution (FEM) simulation with the experimental work conducted by Tamang and Aravindan (2019)

The top surface temperature of the SiC block is measured under microwave irradiation using an infrared pyrometer.

Figure 5A clearly confirms the formation of several electric field resonances for all particle groups in the emulsion phase, resonating the electric field by a factor of 20, 16, and 8 for Geldart A, B, and D particles, respectively. It is worth mentioning that this field enhancement is a strong function of spacing between particles. Smaller gaps generally lead to stronger field enhancements as discussed in detail by McMahon et al.[40] For Geldart D particles, both charge accumulation at the surface and field confinement (capacitive coupling) contribute to the observation of electric field resonances in the emulsion phase, while, for Geldart A and B, it is more due to the field confinement as the charge accumulation at the surface is suppressed for these particles, as can be seen in Figure 1B. The small gap acts as a capacitor-like structure that confines the electric field within a very small volume, leading to a significant enhancement of the local electric field intensity, a phenomenon observed and explained by Liu et al. and Bagiante et al.[41,42] Therefore, according to Figure 5A, we conclude that the emulsion phase of our fluidized bed acts as a capacitor, enhancing the electric field by orders of magnitude and storing the electric energy there.

Conversely, the electric field in the bubble phase of all groups experiences a moderate attenuation through the propagation inside the bed, as depicted in Figure 5B. The electric field norm drops by a factor of 0.8, 0.65, and 0.4 at the center of the bed, where $r/R = 0$, for Geldart A, B, and D particles, respectively. This conspicuously indicates that the electric field interacts differently in the bubble phase compared to the emulsion phase. There is no resonance of the field in the bubble phase to sustain the field.

Figure 5C illustrates the interaction of the magnetic field component with the emulsion phase for all particle groups. Some modes of resonances are observed for Geldart B and D, but not for Geldart A, particles. For instance, the magnetic resonance can be as high as a factor of 1.7 for Geldart D particles, while it is 1.12 and 1.00 for Geldart B and A particles, respectively. Both emulsion and bubble phases in Figures 5C and 5D underscore that the fluidized bed of Geldart A particles has no interaction with the magnetic field. Geldart B particles show a minimal interaction, while Geldart D particles strongly interact with the magnetic field. Figure 5D demonstrates that, similar to the electric field, the magnetic field of Geldart D moderately attenuates as it propagates through the bubble phase.

The comparison of electric and magnetic field behavior seen in Figure 5 suggests that the electric and magnetic components of the microwave interact differently with the fluidized beds of particles. For Geldart A and B particles, according to Figure 5B, the

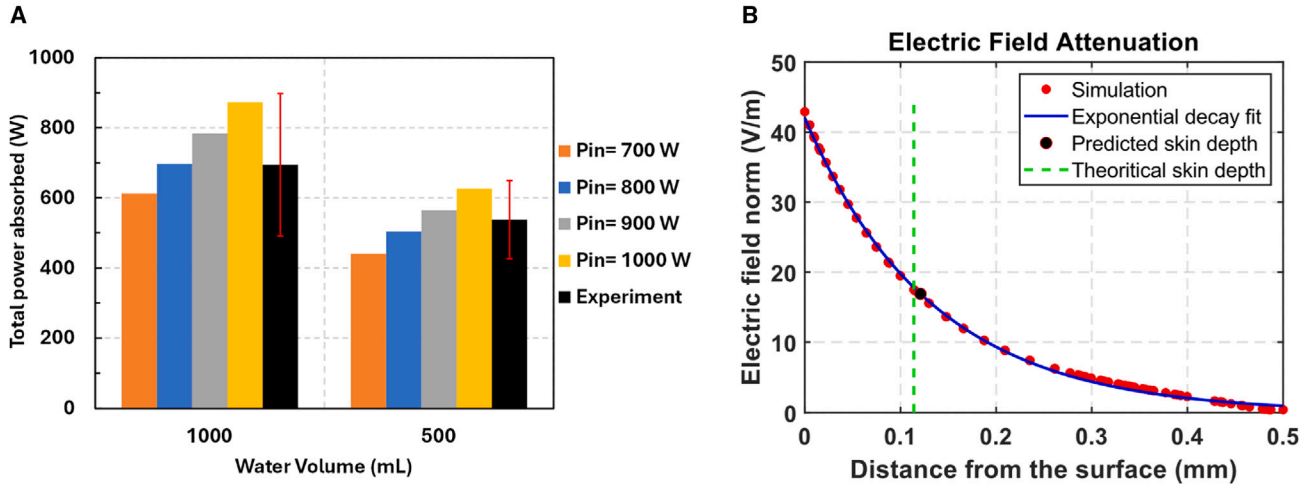

Figure 13. Model assessment of the studied microwave cavity

(A) Comparison of microwave heating absorption of tap water under different conditions.

(B) Validation of skin depth by fitting an exponential decay curve and obtaining the attenuation coefficient of electric field in the carbon particle.

The experimental data are presented as mean ± 200 W and +/− 110 W for 1,000 mL and 500 mL, respectively.

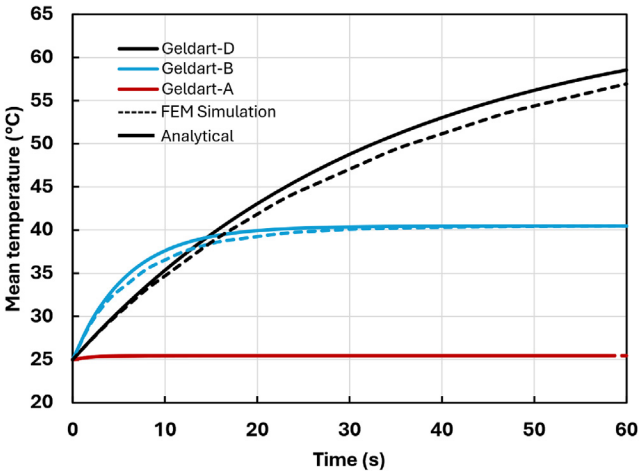

Figure 14. A thermal analysis on the interaction of microwave power absorption with natural convective heat loss for all particle groups under 60 s of microwave irradiation

electric field gradually decreases from both sides as it propagates to the center of the bed, while the magnetic field propagates without any attenuation, as displayed in Figure 5D. Therefore, the present study proposes that the penetration depth may evolve differently under electric and magnetic fields. A similar phenomenon has been observed and reported by Horikoshi et al.,[43] working on the microwave irradiation of aqueous electrolyte solutions. They noted that, with increasing electrolyte concentration, heating rates of aqueous solutions grow nearly exponentially under magnetic field irradiation. However, under electric field irradiation, the heating rates plateau at low concentrations and remain constant with further increase. Nevertheless, this unlocks multiple avenues for future research as the precise understanding of penetration depth under the magnetic component of microwave in a fluidized bed requires large-scale experiments to address this complexity.

Dielectric, semiconductive, or conductive?

As expressed in Equations 9 and 10, microwave heating absorption of any medium depends on the combination of both the EM field strength and material properties. For non-magnetic materials, electrical conductivity plays a key role in determining the mechanism of microwave heating. To explore the effect of electrical conductivity, three distinct types of materials are assigned to the bed of our covered carbon particles, namely, dielectric ($\sigma = 0\ S/m$), semiconductive ($\sigma = 10^4\ S/m$, our case), and conductive ($\sigma = 10^7\ S/m$). Figure 6 compares the performance of microwave heating among these materials for the studied particle groups. It should be noted that the comparison is made relative to the semiconductive case.

Figure 6A indicates that, if our covered carbon particles were dielectric or conductive, the microwave heating would be inefficient, having only a normalized power absorption of 6.3% and 4.8%, respectively, compared to the semiconductive case (actual case). For the fluidized bed of Geldart D particles, dielectric heating becomes comparable to the semiconductive case by having normalized power absorption of 80%. Conductive Geldart A particles, on the other hand, are heated better compared to both dielectric and semiconductive cases. Figures 6B and 6C reveal that, for these particles, the stored electric and magnetic fields in the conductive case account for only 21% and 3.5% of values in the semiconductive case, respectively. However, the induced current density in the conductive Geldart A particles is significantly higher, with a normalized value of 3,500% as shown in Figure 6D. This high current density compensates for the lower strength of the EM field, resulting in a relatively high microwave heating absorption rate of 320% for conductive Geldart A particles, as depicted in Figure 6A.

Overall, Figure 6A demonstrates that Geldart A and B particles are not suitable for the dielectric heating of our fluidized beds. The studied particle sizes are much smaller than a skin depth of 8.2 mm if the particles are dielectric, leading to very small ratios of $d_p/2\delta$. As a result, the microwave penetration depth exceeds the particle size, making these particles transparent to microwaves. Although this results in more uniform heating throughout the particle volume, it reduces the overall heating rate as can be seen in Figure 6A. Thus, it can be deduced that either larger particle sizes are required or a static bed condition might help if the particles are dielectric.

In the conductive case for all particle groups, the incident microwave is reflected as the plots of electric and magnetic fields in Figures 6B and 6C clearly show a negligible accumulation of the EM fields within the particles. For example, the normalized electric field intensity is only 3.5%, 0.5%, and 0.2% for the fluidized beds of Geldart A, B, and D, respectively. It is axiomatic that larger particle sizes result in greater reflection of the EM waves.

Limitations of the study

Figures 7 and 8 show the computational domain and bed configuration used in the current study. Grid independency results are shown in Figure 9. The computational framework is illustrated in Figures 10 and 11. Model validation is shown in Figures 12, 13, and 14. Modeling assumptions and limitations are as follows.

(1) The quartz reactor, the insulating layer, and the gas surrounding particles are treated transparent to EM waves, neither absorbing nor reflecting microwave.
(2) The cavity walls and waveguide are made of copper, with a negligible dielectric loss.
(3) Particles are assumed to be perfectly spherical. In evaluating hotspot intensity at particle contact points, particle shape significantly influences the strength and distribution of EM enhancement. Non-spherical particles, such as particles with sharp corners, tend to generate more intense hotspots compared to spherical particles due to field concentration around edges and corners—a phenomenon well-documented in EM studies.[44] Consequently, assuming spherical particles in our study likely underestimates hotspot intensity. However, even with this approximation, our results (see Figure 2) show that contact points contribute significantly to Joule heating.
(4) The current particle-scale model is primarily limited to the number of particles, capable of modeling 10,000 particles of any size.

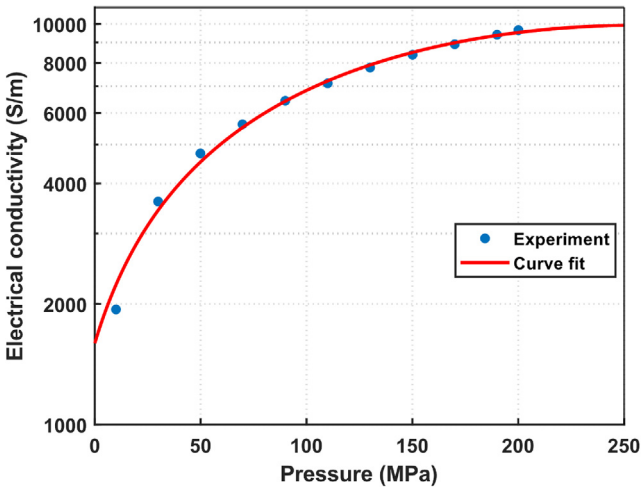

Figure 15. Electrical conductivity measurement of our covered carbon particles under progressive compression using a four-point probe method

(5) It is computationally prohibitive to model the entire bed with Geldart B and A carbon particles as the bed would contain approximately 1.5 and 65 million particles, respectively.
(6) The initial temperature of the particles is set to 25°C.
(7) For heat transfer simulations, thermal, electrical, and dielectric properties of our covered carbon particles are considered constant within the studied temperature range (see Figure 15).

RESOURCE AVAILABILITY

Lead contact

Further information and requests for resources should be directed to and will be fulfilled by the lead contact, Murray J. Thomson (murray.thomson@utoronto.ca).

Materials availability

This study did not generate new unique reagents.

Data and code availability

- All data reported in this paper will be shared by the lead contact upon request.
- The MATLAB code developed to generate a fluidized set of particles is available on the GitHub repository: https://github.com/MehdiSalakhi/BedGeneration.git.
- Any additional information required to reanalyze the data reported in this paper is available from the lead contact upon request.

ACKNOWLEDGMENTS

This work was supported by the Natural Sciences and Engineering Research Council of Canada (NSERC) (grant numbers ALLRP 585024-23 and RGPIN-2020-06136). Additionally, this research was enabled in part by computational resources provided by Calcul Québec (calculquebec.ca) and the Digital Research Alliance of Canada (alliancecan.ca). We gratefully acknowledge CMC Microsystems for providing the products and services, including COMSOL Multiphysics, that facilitated this research.

AUTHOR CONTRIBUTIONS

Conceptualization, M.S. and M.J.T.; methodology, M.S.; software, M.S.; validation, M.S.; formal analysis, M.S.; investigation, M.S. and M.J.T.; resources, M.J.T.; writing – original draft, M.S.; writing – review and editing, M.S. and M.J.T.; visualization, M.S.; supervision, M.J.T.; project administration, M.J.T.; funding acquisition, M.J.T.

DECLARATION OF INTERESTS

M.J.T., a professor at the University of Toronto, is the Chief Science Officer at Aurora Hydrogen.

STAR★METHODS

Detailed methods are provided in the online version of this paper and include the following:

- KEY RESOURCES TABLE
- EXPERIMENTAL MODEL AND STUDY PARTICIPANT DETAILS
- METHOD DETAILS
  - Modeling methodology
  - Model validation
- QUANTIFICATION AND STATISTICAL ANALYSIS

SUPPLEMENTAL INFORMATION

Supplemental information can be found online at https://doi.org/10.1016/j.isci.2024.111732.

Received: August 29, 2024
Revised: November 13, 2024
Accepted: December 30, 2024
Published: January 4, 2025

REFERENCES

1. Ramírez, A.R., and Botero, J.M. (2020). IETS TCP Annex XIX IndustrialElectrification: Task 1 Mapping of Activities, Scoping and Formulation. Delft, Netherlands: of Multiyear Collaboration Plan; Delft University of Technology. https://iea-industry.org/app/uploads/Annex-XIX-report-Task1-FV-1.pdf.
2. Rogelj, J., Shindell, D., Jiang, K., Fifita, S., Forster, P., Ginzburg, V., Handa, C., Kheshgi, H., Kobayashi, S., Kriegler, E., et al. (2022). Mitigation Pathways Compatible with 1.5°C in the Context of Sustainable Development. In Global Warming of 1.5°C. An IPCC Special Report on the impacts of global warming of 1.5°C above pre-industrial levels and related global greenhouse gas emis, pp. 93–174.
3. Roelofsen, O., Somers, K., Speelman, E., and Witteveen, M. (2020). McKinsey & Company - Plugging in: What electrification can do for industry. McKinesy Co, 3–7.
4. Thiel, G.P., and Stark, A.K. (2021). To decarbonize industry, we must decarbonize heat. Joule *5*, 531–550. https://doi.org/10.1016/j.joule.2020.12.007.
5. Yang, W.-C. (2003). Handbook of Fluidization and Fluid-Particle Systems, 1st ed. (CRC Press). https://doi.org/10.1201/9780203912744.
6. Polin, J.P., Peterson, C.A., Whitmer, L.E., Smith, R.G., and Brown, R.C. (2019). Process intensification of biomass fast pyrolysis through autothermal operation of a fluidized bed reactor. Appl. Energy *249*, 276–285. https://doi.org/10.1016/j.apenergy.2019.04.154.
7. Kim, J.Y., Li, Z.J., Jung, H.S., Nam, J.Y., Sung, W.C., Bae, J.W., and Lee, D.H. (2024). Renewable methyl acetate production from dimethyl ether carbonylation in a fluidized bed reactor. Chem. Eng. J. *489*, 151326. https://doi.org/10.1016/j.cej.2024.151326.

8. Ahmed, I., Duchesne, M., Tan, Y., and Lu, D.Y. (2024). Electrically Heated Fluidized Beds—A Review. Ind. Eng. Chem. Res. *63*, 4205–4235. https://doi.org/10.1021/acs.iecr.3c04232.

9. Bai, X., Muley, P.D., Musho, T., Abdelsayed, V., Robinson, B., Caiola, A., Shekhawat, D., Jiang, C., and Hu, J. (2022). A combined experimental and modeling study of Microwave-assisted methane dehydroaromatization process. Chem. Eng. J. *433*, 134445. https://doi.org/10.1016/j.cej.2021.134445.

10. Serra, J.M., Borrás-Morell, J.F., García-Baños, B., Balaguer, M., Plaza-González, P., Santos-Blasco, J., Catalán-Martínez, D., Navarrete, L., and Catalá-Civera, J.M. (2020). Hydrogen production via microwave-induced water splitting at low temperature. Nat. Energy *5*, 910–919. https://doi.org/10.1038/s41560-020-00720-6.

11. El Khaled, D., Novas, N., Gazquez, J.A., and Manzano-Agugliaro, F. (2018). Microwave dielectric heating: Applications on metals processing. Renew. Sustain. Energy Rev. *82*, 2880–2892. https://doi.org/10.1016/j.rser.2017.10.043.

12. Singh, R., Lindenberger, C., Chawade, A., and Vivekanand, V. (2024). Unveiling the microwave heating performance of biochar as microwave absorber for microwave-assisted pyrolysis technology. Sci. Rep. *14*, 9222. https://doi.org/10.1038/s41598-024-59738-5.

13. Luo, C., Liu, S., Yang, G., Jiang, P., Luo, X., Chen, Y., Xu, M., Lester, E., and Wu, T. (2023). Microwave-accelerated hydrolysis for hydrogen production over a cobalt-loaded multi-walled carbon nanotube-magnetite composite catalyst. Appl. Energy *333*, 120538. https://doi.org/10.1016/j.apenergy.2022.120538.

14. Lin, C.H., Wan, C., Ru, Z., Matthew, W., Rivas-davila, J., Fan, J.A., Lin, C.H., Wan, C., Ru, Z., Cremers, C., et al. (2024). Article Electrified thermochemical reaction systems with high-frequency metamaterial reactors Electrified thermochemical reaction systems with high-frequency metamaterial reactors, *8*, pp. 2938–2949. https://doi.org/10.1016/j.joule.2024.07.017.

15. Mallapragada, D.S., Dvorkin, Y., Modestino, M.A., Esposito, D.V., Smith, W.A., Hodge, B.M., Harold, M.P., Donnelly, V.M., Nuz, A., Bloomquist, C., et al. (2023). Decarbonization of the chemical industry through electrification: Barriers and opportunities. Joule *7*, 23–41. https://doi.org/10.1016/j.joule.2022.12.008.

16. Dadsetan, M., Khan, M.F., Salakhi, M., Bobicki, E.R., and Thomson, M.J. (2023). CO2-free hydrogen production via microwave-driven methane pyrolysis. Int. J. Hydrogen Energy *48*, 14565–14576. https://doi.org/10.1016/j.ijhydene.2022.12.353.

17. Cui, Y., Zhang, Y., Cui, L., Xiong, Q., and Mostafa, E. (2023). Microwave-assisted fluidized bed reactor pyrolysis of polypropylene plastic for pyrolysis gas production towards a sustainable development. Appl. Energy *342*, 121099. https://doi.org/10.1016/j.apenergy.2023.121099.

18. Fu, W., Zhang, Y., Cui, L., Liu, H., and Maqsood, T. (2023). Experimental microwave-assisted air gasification of biomass in fluidized bed reactor. Bioresour. Technol. *369*, 128378. https://doi.org/10.1016/j.biortech.2022.128378.

19. Hamzehlouia, S., Shabanian, J., Latifi, M., and Chaouki, J. (2018). Effect of microwave heating on the performance of catalytic oxidation of n-butane in a gas-solid fluidized bed reactor. Chem. Eng. Sci. *192*, 1177–1188. https://doi.org/10.1016/j.ces.2018.08.054.

20. Cui, Y., Zhang, Y., Cui, L., Zhao, W., and Faizan, A. (2023). Microwave heating of silicon carbide and polypropylene particles in a fluidized bed reactor. Appl. Therm. Eng. *232*, 121009. https://doi.org/10.1016/j.applthermaleng.2023.121009.

21. Karches, M., Takashima, H., and Kanno, Y. (2004). Development of a circulating fluidized-bed reactor for microwave-activated catalysis. Ind. Eng. Chem. Res. *43*, 8200–8206. https://doi.org/10.1021/ie049569p.

22. Di Liddo, L., Cepeda, F., Saegh, G., Salakhi, M., and Thomson, M.J. (2024). Comparative analysis of methane and natural gas pyrolysis for low-GHG hydrogen production. Int. J. Hydrogen Energy *84*, 146–154. https://doi.org/10.1016/j.ijhydene.2024.08.190.

23. Zeng, X., Cheng, X., Yu, R., and Stucky, G.D. (2020). Electromagnetic microwave absorption theory and recent achievements in microwave absorbers. Carbon N. Y. *168*, 606–623. https://doi.org/10.1016/j.carbon.2020.07.028.

24. Mohd Mokhta, Z., Ong, M.Y., Salman, B., Nomanbhay, S., Salleh, S.F., Chew, K.W., Show, P.L., and Chen, W.H. (2020). Simulation studies on microwave-assisted pyrolysis of biomass for bioenergy production with special attention on waveguide number and location. Energy *190*, 116474. https://doi.org/10.1016/j.energy.2019.116474.

25. Gangurde, L.S., Sturm, G.S.J., Devadiga, T.J., Stankiewicz, A.I., and Stefanidis, G.D. (2017). Complexity and Challenges in Noncontact High Temperature Measurements in Microwave-Assisted Catalytic Reactors. Ind. Eng. Chem. Res. *56*, 13379–13391. https://doi.org/10.1021/acs.iecr.7b02091.

26. Mishra, R.R., and Sharma, A.K. (2016). Microwave-material interaction phenomena: Heating mechanisms, challenges and opportunities in material processing. Composer Part A Appl. Sci. Manuf. *81*, 78–97. https://doi.org/10.1016/j.compositesa.2015.10.035.

27. Haneishi, N., Tsubaki, S., Abe, E., Maitani, M.M., Suzuki, E.I., Fujii, S., Fukushima, J., Takizawa, H., and Wada, Y. (2019). Enhancement of Fixed-bed Flow Reactions under Microwave Irradiation by Local Heating at the Vicinal Contact Points of Catalyst Particles. Sci. Rep. *9*, 222. https://doi.org/10.1038/s41598-018-35988-y.

28. Rybakov, K.I., Semenov, V.E., Egorov, S.V., Eremeev, A.G., Plotnikov, I.V., and Bykov, Y.V. (2006). Microwave heating of conductive powder materials. J. Appl. Phys. *99*. https://doi.org/10.1063/1.2159078.

29. Choy, T.C. (2015). Effective Medium Theory Principles and Applications (Oxford University Press), pp. 9–18.

30. Goyal, H., and Vlachos, D.G. (2020). Multiscale modeling of microwave-heated multiphase systems. Chem. Eng. J. *397*, 125262. https://doi.org/10.1016/j.cej.2020.125262.

31. Ignatenko, M., Tanaka, M., and Sato, M. (2009). Absorption of microwave energy by a spherical nonmagnetic metal particle. Jpn. J. Appl. Phys. *48*, 067001. https://doi.org/10.1143/JJAP.48.067001.

32. Salakhi, M., Cepeda, F., and Thomson, M.J. (2024). A comprehensive kinetic study on low-GHG hydrogen production from microwave-driven methane pyrolysis. Int. J. Hydrogen Energy *77*, 997–1008. https://doi.org/10.1016/j.ijhydene.2024.06.259.

33. Cocco, R., Karri, S.B.R., and Knowlton, T. (2014). Introduction to fluidization. Chem. Eng. Prog. *110*, 21–29.

34. Fidalgo, B., Fernández, Y., Domínguez, A., Pis, J.J., and Menéndez, J.A. (2008). Microwave-assisted pyrolysis of CH4/N2 mixtures over activated carbon. J. Anal. Appl. Pyrolysis *82*, 158–162. https://doi.org/10.1016/j.jaap.2008.03.004.

35. Wen, M., Liu, Y., Ren, J., Wang, J., and Jiang, J. (2024). Optimizing microwave frequencies for hydrogen and electromagnetic shielding materials production through methane pyrolysis over biochar. Energy Convers. Manag. *309*, 118430. https://doi.org/10.1016/j.enconman.2024.118430.

36. Patlolla, S.R., Katsu, K., Sharafian, A., Wei, K., Herrera, O.E., and Mérida, W. (2023). A review of methane pyrolysis technologies for hydrogen production. Renew. Sustain. Energy Rev. *181*, 113323. https://doi.org/10.1016/j.rser.2023.113323.

37. Amini, A., Ohno, K., Maeda, T., and Kunitomo, K. (2018). Effect of particle size and apparent density on the initial stages of temperature increase during the microwave heating of Fe3O4. Powder Technol. *338*, 101–109. https://doi.org/10.1016/j.powtec.2018.06.047.

38. Yoshikawa, N., Ishizuka, E., and Taniguchi, S. (2006). Heating of metal particles in a single-mode microwave applicator. Mater. Trans. *47*, 898–902. https://doi.org/10.2320/matertrans.47.898.

39. Grace, J.R., Chaouki, J., and Pugsley, T. (2016). Fluidized bed reactor. https://doi.org/10.1016/b978-0-12-410416-7.00008-2.

40. McMahon, J.M., Li, S., Ausman, L.K., and Schatz, G.C. (2012). Modeling the effect of small gaps in surface-enhanced Raman spectroscopy. J. Phys. Chem. C *116*, 1627–1637. https://doi.org/10.1021/jp207661y.

41. Liu, C., Wang, C., Chen, J., Su, Y., Qiao, L., Zhou, J., and Bai, Y. (2022). Ultrasensitive Frequency Shifting of Dielectric Mie Resonance near Metallic Substrate. Research *2022*, 9862974. https://doi.org/10.34133/2022/9862974.

42. Bagiante, S., Enderli, F., Fabiańska, J., Sigg, H., and Feurer, T. (2015). Giant electric field enhancement in split ring resonators featuring nanometer-sized gaps. Sci. Rep. *5*, 8051. https://doi.org/10.1038/srep08051.

43. Horikoshi, S., Sumi, T., and Serpone, N. (2012). Unusual effect of the magnetic field component of the microwave radiation on aqueous electrolyte solutions. J. Microw. Power Electromagn. Energy *46*, 215–228. https://doi.org/10.1080/08327823.2012.11689838.

44. Lu, Y., Liu, G.L., Kim, J., Mejia, Y.X., and Lee, L.P. (2005). Nanophotonic crescent structures with sharp edge for ultrasensitive biomolecular detections by local electromagnetic field enhancement effect. In Micro Total Anal. Syst. - Proc. MicroTAS 2005 Conf. 9th Int. Conf. Miniaturized Syst. Chem. Life Sci., *1*, pp. 1230–1233.

45. Walter Frei (2020). Computational Electromagnetics Modeling: Which Module to Use?. https://www.comsol.com/blogs/computational-electromagnetics-modeling-which-module-to-use.

46. Mehdizadeh, M. (2015). The impact of fields on materials at microwave and radio frequencies, pp. 1–33. https://doi.org/10.1016/b978-0-323-32256-0.00001-4.

47. Vashisth, A., Upama, S.T., Anas, M., Oh, J.H., Patil, N., and Green, M.J. (2021). Radio frequency heating and material processing using carbon susceptors. Nanoscale Adv. *3*, 5255–5264. https://doi.org/10.1039/d1na00217a.

48. Geldart, D. (1973). Elsevier Sequoia SA, Lausanne-Printed in the Netherlands Types of Gas Fhidization. Powder Technol. *7*, 285–292.

49. Buchelnikov, V.D., Louzguine-Luzgin, D.V., Xie, G., Li, S., Yoshikawa, N., Sato, M., Anzulevich, A.P., Bychkov, I.V., and Inoue, A. (2008). Heating of metallic powders by microwaves: Experiment and theory. J. Appl. Phys. *104*. https://doi.org/10.1063/1.3009677.

50. Manière, C., Lee, G., Zahrah, T., and Olevsky, E.A. (2018). Microwave flash sintering of metal powders: From experimental evidence to multiphysics simulation. Acta Mater. *147*, 24–34. https://doi.org/10.1016/j.actamat.2018.01.017.

51. Crane, C.A., Pantoya, M.L., Weeks, B.L., and Saed, M. (2014). The effects of particle size on microwave heating of metal and metal oxide powders. Powder Technol. *256*, 113–117. https://doi.org/10.1016/j.powtec.2014.02.008.

52. Cheng, J., Roy, R., and Agrawal, D. (2002). Radically different effects on materials by separated microwave electric and magnetic fields. Mater. Res. Innovat. *5*, 170–177. https://doi.org/10.1007/s10019-002-8642-6.

53. Jeon, S., Kim, J., and Yang, D. (2022). Design of Large-Scale Microwave Cavity for Uniform and Efficient Plastic Heating. Polymers *14*, 541. https://doi.org/10.3390/polym14030541.

54. Santos, T., Costa, L., and Valente, M. (2010). 3D electromagnetic field simulation in microwave ovens: a tool to control thermal runaway. Proc. COMSOL Conf. 2010 Paris, 3–7.

55. Manzoor, S., Wani, O.B., and Bobicki, E.R. (2024). Investigating the microwave properties of carbon materials from microwave-driven methane pyrolysis. Carbon Trends *14*, 100326. https://doi.org/10.1016/j.cartre.2024.100326.

56. Digital Research Alliance of Canada. https://docs.alliancecan.ca/wiki/Narval/en.

57. Tamang, S., and Aravindan, S. (2019). 3D numerical modelling of microwave heating of SiC susceptor. Appl. Therm. Eng. *162*, 114250. https://doi.org/10.1016/j.applthermaleng.2019.114250.

58. Vollmer, M. (2004). Physics of the microwave oven. Phys. Educ. *39*, 74–81. https://doi.org/10.1088/0031-9120/39/1/006.

59. Vyas, S.K., Verma, R.K., Maurya, S., and Singh, V.V.P. (2016). Review of Magnetron Developments. Frequenz *70*, 455–462. https://doi.org/10.1515/freq-2015-0196.

60. Akimov, Y. (2022). Theory of electromagnetic fields. Emergent Micro Nanomater. Opt. Infrared, Terahertz Appl., 23–60. https://doi.org/10.1201/9781003202608-2.

61. Gezahegn, Y.A., Tang, J., Sablani, S.S., Pedrow, P.D., Hong, Y.K., Lin, H., and Tang, Z. (2021). Dielectric properties of water relevant to microwave assisted thermal pasteurization and sterilization of packaged foods. Innovat. Food Sci. Emerg. Technol. *74*, 102837. https://doi.org/10.1016/j.ifset.2021.102837.

STAR★METHODS

KEY RESOURCES TABLE

REAGENT or RESOURCE	SOURCE	IDENTIFIER
Software and algorithms		
COMSOL Multiphysics v62	COMSOL, Inc	https://www.comsol.com/
BedGeneration.m	Mehdi Salakhi	https://github.com/MehdiSalakhi/BedGeneration.git

EXPERIMENTAL MODEL AND STUDY PARTICIPANT DETAILS

This study didn't use any experimental model.

METHOD DETAILS

Modeling methodology

Maxwell's equations are a set of four fundamental laws that describe the propagation of electric and magnetic fields and their interactions with matter. The differential forms are written as follows:

$$\nabla.D = \rho_v \quad \text{(Equation 1)}$$

$$\nabla.B = 0 \quad \text{(Equation 2)}$$

$$\nabla \times E = -\frac{\partial B}{\partial t} \quad \text{(Equation 3)}$$

$$\nabla \times H = \frac{\partial D}{\partial t} + J \quad \text{(Equation 4)}$$

where D is the electric flux density (C/m^2), ρ_v is the electric charge density (C/m^3), B is the magnetic flux density (Wb/m^2), E is the electric field (V/m), H is the magnetic field (A/m), and J is the current density (A/m^2).

Resonant cavities like microwave involve time-harmonic fields that oscillate sinusoidally at specific frequencies.[45] Frequency domain analysis is efficient and well-suited for such problems. Therefore, the frequency domain form is utilized in the current model. To this end, the above Maxwell's equations are transformed using the Fourier analysis into frequency domain, simplifying the problem by converting time-dependent differential equations into algebraic equations. Consequently, the following form of the Maxwell's equation is solved numerically:

$$\nabla \times \left(\mu_r^{-1} \nabla \times E\right) - \omega^2 \epsilon_0 \mu_0 \left(\varepsilon_r - \frac{j\sigma}{\omega \varepsilon_0}\right) E = 0 \quad \text{(Equation 5)}$$

where μ_r is the relative permeability, ω is the angular frequency (rad/s), ε_r is the relative permittivity, σ is the electrical conductivity (S/m), ε_0 (F/m) and μ_0 (H/m) are the vacuum permittivity and permeability, respectively. Equation (Equation 5 is explicitly written in terms of the electric field, subsequently, the magnetic field is computed by the following expression:

$$j\omega B = \nabla \times E \quad \text{(Equation 6)}$$

The current density, J in Equation 4, is related to the magnetic field by:

$$\overline{J} = (\sigma + j\omega\varepsilon_0\varepsilon_r)\overline{E} \quad \text{(Equation 7)}$$

Electric currents within materials have two main components. The first is the conductivity component, which results in the conduction current that is essentially independent of operating frequency. Conductivity represents the portion of electrical current responsible for the movement of free charges within the material, frequently colliding with subatomic particles and causing Joule or resistive heating.[46]

The second type of current arises when an electric field is applied to the material, causing polarization due to the rotation or finite displacement of charges (electrons) within the material. This polarization generates currents associated with the material's permittivity, leading to dielectric heating.[47]

The permittivity is represented in a complex algebraic format as below:

$$\varepsilon_r = \varepsilon_r' - j\varepsilon_r'' \quad \text{(Equation 8)}$$

where ε_r' is the dielectric constant which determines the ability of a material to store electrical energy and ε_r'' is the dielectric loss factor, representing the energy dissipation as heat.

The electric current density is then computed as below:

$$\overline{J} = \left(\sigma + \omega\varepsilon_0\varepsilon_r''\right)\overline{E} + j\omega\varepsilon_0\varepsilon_r'\overline{E} \quad \text{(Equation 9)}$$

The first term on the right-hand side represents the dissipation of EM energy into heat within the material due to the current, taking both dielectric and Joule heating into account. The second term is the reactive component of the current, which exhibits a phase lag with respect to the imposed electric field. This reactive current, often called the displacement current, does not follow the electric field instantly, lagging by a certain phase angle. Unlike conduction current, it does not contribute to power dissipation in the material.[46]

It should be noted that since our carbon particles are non-magnetic, the heat generation from magnetic losses is negligible. Therefore, the total microwave power absorption density, P_{MW} (W/m^3), can be expressed by the real part of the dot product of current density and complex conjugate of the electric field vector, E^*, as follows:

$$P_{MW} = \frac{1}{2}Re(J.E^*) \quad \text{(Equation 10)}$$

To quantitatively evaluate the uniformity in microwave heating, the coefficient of variation, $COVP_{MW}$, for microwave power absorption density is defined as:

$$COVP_{MW} = \frac{1}{\overline{P}_{MW}}\sqrt{\frac{1}{N}\sum_{i=1}^{N}\left(P_{MWi} - \overline{P}_{MW}\right)^2} \quad \text{(Equation 11)}$$

where $\overline{P}_{MW}$ is the mean of volume average power absorption density of all particles, P_{MWi} is the volume average power absorption density of a certain particle i, and N is the number of particles in the bed. Statistically, a higher COV means greater non-uniformity in heating

Based on the conservation of energy, the following unsteady energy equation is solved for each individual particle:

$$\rho_c c_p\frac{\partial T}{\partial t} + \nabla.(-k_c\nabla T) = P_{MW} \quad \text{(Equation 12)}$$

where T is the temperature (K), c_p is the specific heat capacity ($J/kg.K$), ρ_c (kg/m^3) and k_c ($W/m.K$) are the density and thermal conductivity of the carbon particles, respectively.

Figure 7 illustrates the microwave heating of the fluidized bed of our carbon particles. Experiments[16] were performed in a 1-inch reactor with a length of 10 inch in a multimode microwave cavity operating at 2.45 GHz purchased from Microwave Research & Applications. Inc, as schematically shown in Figure 7A. The microwave oven was positioned vertically, and the quartz reactor was placed with a coordinate shown in Figure 7B inside the cavity. The power level was set to 65-75 during the experiments, supplying almost 500 W of microwave power to the cavity. As can be seen in Figure 7A, a k-type thermocouple was inserted from the top, placed at the center of the bed, and connected to the LabVIEW system, recording the real-time local temperature.

The computational domain consists of a multimode microwave cavity, waveguide, and a fluidized bed, as illustrated in Figure 7B. As shown, a microwave cavity with 330 mm height, 330 mm depth, and 205 mm width combined with a rectangular waveguide with a dimension of 78 mm × 18 mm and width of 50 mm is modeled to study our multimode cavity. According to the intrinsic density of our carbon particles (~1900 kg/m^3),[32] three representative particle sizes are selected based on Geldart's particle classification in the field of fluidization: 100 μm (Geldart A), 350 μm (Geldart B – our experiment), and 2000 μm (Geldart D).[48] The bed is entirely filled with Geldart D particles, allowing us to study the microwave interaction with matter at both particle and bulk (bed) levels. It should be noted that due to computational constraints, a smaller bed size is employed to model Geldart A and B particles, with dimensions displayed in Figure 8. This chosen bed size falls within the range of many experimental works on microwave heating of micro/nano powders.[27,49–52]

For effective and accurate microwave heating simulations, it is recommended to use a mesh element size that is a small fraction of the microwave wavelength, ensuring a reasonable resolution for the electromagnetic (EM) field.[53] When the EM waves interact with non-magnetic matter, the effective wavelength inside a material (λ_{eff}) is related to the material's permittivity, ε', by the equation $\lambda_{eff} = \lambda_0/\sqrt{\varepsilon'}$, where λ_0 is the free space wavelength. This means that as the permittivity of the load increases, the effective wavelength decreases, which requires smaller mesh elements.[54] Given that the particles under study are significantly smaller than the effective wavelength of ~1.5 cm, the maximum element size within each particle is chosen to be a small fraction of the particle size. Consequently, the cavity is meshed based on the wavelength of the microwave, while the particles are meshed according to their size. It should be noted that 10 boundary layers are applied only to Geldart D particles to resolve the effect of skin depth, which is around 0.1 mm. A single layer of mesh refinement is used for the bed region to avoid low-quality

elements due to the presence of thin regions between particles. However, a couple of low-quality elements were inevitable when dealing with our complex geometry. Nevertheless, maintaining an average element quality greater than 0.66 promotes the convergence of the solution, The minimum element size below 10 μm ensures that the narrow regions are sufficiently resolved.

Details of the generated mesh for the particle scale simulations

Particle bed	Number of elements	Average element quality	Minimum element size (μm)
Geldart D (2 mm)	50,195,207	0.662	10
Geldart B (0.35 mm)	51,249,565	0.663	8
Geldart A (0.1 mm)	54,947,285	0.664	4

Given this, three element sizes of 30%, 15%, and 10% of the wavelength/particle size are tested, leading to a total number of ∼ 10, 50, and 100 million elements, respectively. It is worthy to note that the simulation cases with over 100 million elements were performed using 3 nodes with a total of 192 cores in parallel configuration. Figure 9 compares the average of power absorption density across the bed among the selected element sizes for all particle groups. The grid sensitivity analysis discloses that an element size lower than 15% improves the accuracy only by 3%, 2.5%, and 4.4% with respect to the finest mesh for Geldart D, B, and A particles, respectively. Therefore, a maximum element size of 15% of the wavelength in the cavity and 15% of the corresponding particle size within each particle can guarantee a mesh-independent solution and is used for the simulations.

As shown in Figure 15, although even under a significant pressure like 200 MPa some degree of contact resistance and remaining porosity persist, it is reasonable to assume that the measurements could closely represent single particle conductivity. Therefore, according to the fitted curve shown in Figure 15, the intrinsic electrical conductivity of the covered carbon particles is set to 10^4 S/m in the simulations. The effective (bulk) dielectric properties of our covered carbon particles in a loose powder are taken from the experimental measurements in.[55] In the loose powder, the bulk solid volume fraction of our carbon bed roughly equals to 0.455. The intrinsic dielectric properties of the particles are then calculated based on the Bruggeman's model as follows[29]:

$$\alpha_s \frac{\varepsilon_c - \varepsilon_{eff}}{\varepsilon_c + 2\varepsilon_{eff}} + (1 - \alpha_s) \frac{\varepsilon_{gas} - \varepsilon_{eff}}{\varepsilon_{gas} + 2\varepsilon_{eff}} = 0 \quad \text{(Equation 13)}$$

where α_s is the solid volume fraction, ε_{eff} is the effective dielectric of the carbon bed, ε_c and ε_{gas} is the intrinsic permittivity of carbon particles and the gas (air) surrounding them, respectively.

EM properties of the material used in the present study.

Material	$\sigma\ (S/m)$	ε_r'	ε_r''	μ_r'	μ_r''
Carbon particle	10,000	63.7	39.5	1	0
Gas (air)	0	1	0	1	0

The port boundary condition is used at the entrance of the rectangular waveguide, as displayed in Figure 7B. The waveguide operates in the transverse electric TE10 mode and is excited at a frequency of 2.45 GHz. In all simulations involving particles, the port input power is set to 500 W.

The impedance boundary condition (IBC) is applied to all the walls of cavity and its waveguide, which is useful at boundaries where the EM field penetrates only a short distance outside the boundary. This provides a simple model to take the heat loss due to skin depth in the walls into account without needing to solve the Maxwell's equations at the boundary. The following mathematical expression is solved at the conductive walls of the cavity and waveguide:

$$E_t = \sqrt{\frac{j\mu_0\mu_r\omega}{\sigma}} H_t \times n \quad \text{(Equation 14)}$$

where n is the unit normal vector to the surface and E_t and H_t are the tangential component of the electric and magnetic fields at the boundary surface, respectively.

Two heat flux thermal boundary conditions are applied to the surface of each particle.

Thermal boundary conditions and parameters employed in the present model		
Condition	Insulation	Natural convective heat loss
Heat flux $\dot{q}$ (W/m^2)	$\dot{q} = 0$	$\dot{q} = h(T_{ambient} - T_s)$
Ambient temperature $T_{ambient}$ (°C)	25	
Heat transfer coefficient h (W/m^2.K)	15	

The implemented computational procedure is summarized in Figure 10. A fluidized bed of particles is achieved by coupling MATAB R2023a with the COMSOL Multiphysics v6.2 through the LiveLink interface. A fluidized bed is generated by randomly distributing particles confined in a cylindrical bed based on the bed dimension, particle size, and bulk solid volume fraction. A collision detection is defined by calculating the distance between the particle centroids to preclude particles from having contact points, resulting in a fluidized state for all the particles. Afterwards, the simulation case is completed in the COMSOL environment. The current particle scale model is memory limited. Therefore, the GMRES iterative solver is used to solve the linear equation systems obtained from the discretization of Equation 5, which requires significantly less memory than a direct solver for the same sized problem. All of the fluidized bed simulations were performed by implementing High-Performance Computing (HPC) on the Narval cluster, running in the distributed mode on the AMD EPYC 64-core processor with an available total memory of 2063.71 GB.[56]

Furthermore, a one-way frequency-transient model is employed to couple the Maxwell's equation with the Energy equation, obtaining the distribution of the temperature for simulation cases where heat transfer equation is solved. This coupling algorithm initially solves Maxwell's equation in the frequency domain, and then passes the power absorption density data to the Heat Transfer module in the COMSOL. More details are provided in Figure 11.

Model validation

Although experiments play a critical role in investigating our microwave heating process, the distributions of EM and temperature fields are problematic to physically measure in our process because of the complex microwave interaction, particle dynamics, and fluid flow occurring simultaneously. Nonetheless, three distinct levels of verification are tested to assure confidence and accuracy in the present study.

We first aim to reproduce the experimental results performed by Tamang and Aravindan,[57] where they experimentally and numerically studied the microwave heating of SiC susceptor. They measured the temperature at the center of the top surface of the SiC cylinder in a multimode microwave cavity using an infrared thermometer. As depicted in Figure 12, the simulation showcases an excellent agreement with their experimental measurements. This gives confidence in using COMSOL simulations to model microwave heating in our multimode cavity.

The performance of our 1 kW microwave cavity with its waveguide is validated using tap water tests with two volumes of 500 mL and 1000 mL. Due to the uncertainty in the delivered microwave power into the cavity, four different levels of microwave input power of 700, 800, 900, and 1000 W are employed in the simulations. Figure 13A compares the total microwave power absorption between the experiment and the simulations. As can be seen, the simulation result of 800 W of input power shows the best agreement with the power absorption calculated from the experiments. Figure 13A also suggests that the microwave potentially delivers 800 W of power to the cavity when the power level is set to 100, which is 80% of the microwave's rated power, aligning well with the typical microwave performance in the literature.[58,59]

Additionally, the particle-scale model is validated against the theoretical electromagnetics. For this purpose, skin depth obtained from a single particle irradiated by microwaves in the studied cavity is compared to the theoretical skin depth. From theory, skin depth is the distance where the intensity of the EM field is exponentially attenuated by $1/e$ (36.8%) of its value at the surface. This exponential attenuation in a spherical coordinate can be mathematically described as[60]:

$$E = E_0 e^{-\alpha r} \quad \text{(Equation 15)}$$

where E is the electric field norm at a distance r into the particle, E_0 is the norm of the electric field at the surface, and α is the attenuation coefficient. Skin depth is the reciprocal of the attenuation coefficient, and for a highly lossy medium, where $\sigma / \omega\varepsilon_0\varepsilon_r >> 1$, the skin depth, δ, equals to[26]:

$$\delta = \frac{1}{\alpha} = \sqrt{\frac{1}{\pi f \mu_0 \mu_r \sigma}} \quad \text{(Equation 16)}$$

Theoretical skin depth obtained from above is equal to 0.114 mm. Figure 13B shows the exponential attenuation of the electric field as it propagates through the particle. According to Equation 15, an exponential curve is fitted to the simulation results to obtain the attenuation rate. Consequently, the simulation results in a skin depth of 0.121 mm, leading to a relatively small error of 6%. This shows the predictive capability of the particle scale model implemented in the current study.

Since liquid water strongly couples with microwave, water test is a simple yet efficient solution to estimate the available microwave power. This approach is also useful in simulations to accurately determine the distribution of electric and magnetic fields within the

cavity. For this purpose, two volumes of water, 1000 mL and 500 mL, are placed at the center of the vertically-oriented microwave oven. A setup similar to that shown in Figure 7 is used to conduct the microwave heating of the tap water samples. After heating, the final temperature is measured after pouring the water into another clean beaker, allowing for more accurate estimation of the average temperature. The dielectric properties of the tap water sample used for the simulations are obtained from.[61]

In the experiments, the temperature measurement uncertainty (ΔT) is computed as below:

$$\Delta T = \sqrt{(\Delta T_{thermocouple})^2+(\Delta T_{std})^2} \quad \text{(Equation 17)}$$

where $\Delta T_{thermocouple}$ is the thermocouple uncertainty reported to be $\pm 2.5^{\circ}$C by the manufacturer and ΔT_{std} is the standard deviation in the temperature measurements, considered to be 1°C.

It is a well-established fact that when water is placed in a glass or plastic container, the surface forms a curved shape known as a meniscus. The volume of tap water samples is measured using a beaker and reading the bottom of the meniscus to minimize the errors associate with readings. Nevertheless, the uncertainty in the markings on the beaker is about ±5% of the volume of the container. Combing the uncertainties involved in temperature and volume measurements bring about 200 W and 110 W of uncertainty in the calculation of total power absorption for water volumes of 1000 mL and 500 mL, respectively. The uncertainty associated with the properties of water is neglected within the operating temperature range. Table S1 summarizes the details of the water test in our microwave cavity under 60 s of microwave heating.

Lumped capacitance approximation is valid for our particle scale study as the Biot number, with the thermal properties provided in Table S2 and a natural convective coefficient of 15 W/m^2.K, is below 0.1 for all particle groups. Thus, applying the energy equation to a spherical particle exposed to ambient and irradiated by microwave leads to the following first-order ordinary differential equation (ODE):

$$\rho_p c_p \frac{dT_p}{dt} = P_{MW} - \frac{6h}{d_p}(T_p - T_{ext}) \quad \text{(Equation 18)}$$

where,

$$T_p(0) = T_{ext} = 298.15\,K$$

where T_p is the particle temperature (K), T_{ext} is the surrounding temperature, h is the natural convective heat transfer coefficient ($W/m^2.K$), P_{MW} is the power absorption density (W/m^3), d_p is the particle size (m), t is the time (s), and ρ_p and c_p are the density (kg/m^3) and specific heat capacity ($J/kg.K$) of the particle, respectively. Solving the above ODE equation with its initial boundary condition results in the following expression for the particle temperature:

$$T_p(t) = T_{ext} + \frac{P_{MW}}{\pi h d_p^2}\left(1 - \exp\left(-\frac{6h}{\rho_p c_p d_p}t\right)\right) \quad \text{(Equation 19)}$$

The evolution of particle temperature over time obtained from the above equation and FEM COMOSOL simulations is plotted in Figure 14. As can be seen, the simulations agree with the analytical model, with a maximum relative error of only 3.5% observed for Geldart D particles. This validates the numerically solved heat transfer equation for each particle in the simulations.

QUANTIFICATION AND STATISTICAL ANALYSIS

There are no statistical analysis or quantification to include in this study.